



# Circumstellar Disk Accretion Across the Lagoon Nebula: The Influence of Environment and Stellar Mass

Laura Venuti<sup>1,2</sup>, Ann Marie Cody<sup>1</sup>, Giacomo Beccari<sup>3</sup>, Luisa M. Rebull<sup>4</sup>, Michael J. Irwin<sup>5</sup>, Apoorva Thanvantri<sup>6</sup>, Sowmya Thanvantri<sup>7</sup>, Silvia H. P. Alencar<sup>8</sup>, Clara O. Leal<sup>8</sup>, Geert Barentsen<sup>9,10</sup>, Janet E. Drew<sup>11</sup>, and Steve B. Howell<sup>10</sup>

<sup>1</sup>SETI Institute, 339 Bernardo Ave., Suite 200, Mountain View, CA 94043, USA; [lvenuti@seti.org](mailto:lvenuti@seti.org)

<sup>2</sup>CSSM and Department of Physics, University of Adelaide, North Terrace campus, Adelaide, SA 5005, Australia

<sup>3</sup>European Southern Observatory, Karl-Schwarzschild-Strasse 2, 85748 Garching bei München, Germany

<sup>4</sup>Infrared Science Archive (IRSA), IPAC, 1200 E. California Blvd., California Institute of Technology, Pasadena, CA 91125, USA

<sup>5</sup>Institute of Astronomy, University of Cambridge, Madingley Road, Cambridge CB3 0HA, UK

<sup>6</sup>California Institute of Technology, 1200 East California Blvd., Pasadena, CA 91125, USA

<sup>7</sup>University of California, Berkeley, 101 Sproul Hall, Berkeley, CA 94720, USA

<sup>8</sup>Departamento de Física—ICEx—UFMG, Av. Antônio Carlos 6627, 30270-901 Belo Horizonte, MG, Brazil

<sup>9</sup>Bay Area Environmental Research Institute, P.O. Box 25, Moffett Field, CA 94035, USA

<sup>10</sup>NASA Ames Research Center, Moffett Field, CA 94035, USA

<sup>11</sup>Department of Physics & Astronomy, University College London, Gower Street, London, WC1E 6BT, UK

Received 2023 September 18; revised 2023 December 18; accepted 2024 January 8; published 2024 February 20

## Abstract

Pre-main-sequence disk accretion is pivotal for determining the final stellar properties and the early conditions for close-in planets. We aim to establish the impact of internal (stellar mass) and external (radiation field) parameters on the disk evolution in the Lagoon Nebula massive star-forming region. We employ simultaneous  $u$ ,  $g$ ,  $r$ ,  $i$ ,  $H\alpha$  time-series photometry, archival infrared data, and high-precision K2 light curves to derive the stellar, disk, and accretion properties for 1012 Lagoon Nebula members. We estimate that of all young stars in the Lagoon Nebula, 34%–37% have inner disks traceable down to  $\sim 12 \mu\text{m}$ , while 38%–41% are actively accreting. We detect disks  $\sim 1.5$  times more frequently around G, K, and M stars than around higher-mass stars, which appear to deplete their inner disks on shorter timescales. We find tentative evidence for a faster disk evolution in the central regions of the Lagoon Nebula, where the bulk of the O/B population is located. Conversely, disks appear to last longer at the nebula outskirts, where the measured fraction of disk-bearing stars tends to exceed that of accreting and disk-free stars. The derived mass accretion rates show a nonuniform dependence on stellar mass between  $\sim 0.2$  and  $5 M_{\odot}$ . In addition, the typical accretion rates appear to differ across the Lagoon Nebula extension, with values twice lower in the core region than at its periphery. Finally, we detect tentative radial density gradients in the surface accretion shocks, leading to lags in the appearance of light curve brightness features as a function of wavelength that can amount to  $\sim 7\%$ – $30\%$  of the rotation period.

*Unified Astronomy Thesaurus concepts:* Stellar accretion disks (1579); Young stellar objects (1834); Star forming regions (1565); T Tauri stars (1681); Herbig Ae/Be stars (723); Variable stars (1761); Light curves (918); Multi-color photometry (1077)

*Supporting material:* machine-readable table

## 1. Introduction

During the first few million years (Myr) after the early formation stages, the evolution of young stars is governed by the interaction with their surrounding protoplanetary disks (e.g., Bouvier et al. 2007). This stage plays a long-lasting role in the determination of the fundamental properties of the final star, and the dynamical star–disk interaction can affect both the survival and orbital configuration of close-in planets (Liu et al. 2017; Romanova et al. 2019). For solar-type and lower-mass young stellar objects (YSOs), the inner regions of the circumstellar disk are truncated at a distance of a few stellar radii from the central source (e.g., Eisner et al. 2014; Gravity Collaboration et al. 2020) as a result of the pressure exerted by the intense ( $\sim \text{kG}$ ) magnetic field at the surface of the star (e.g., Yang & Johns-Krull 2011; Johnstone et al. 2014; Lavail et al. 2017). The stellar magnetosphere therefore controls the

exchange of mass and angular momentum between the star and the inner disk via the process of magnetospheric accretion (Hartmann et al. 2016). This mechanism may also be operating in some higher-mass YSOs (for which the detection of magnetic fields is less common; e.g., Alecian et al. 2013; Villebrun et al. 2019), as suggested by the observation of rotationally modulated line emission signatures (e.g., Pogodin et al. 2021; Brittain et al. 2023) characteristic of magnetospheric accretion streams (e.g., Kurosawa et al. 2011).

Determining the time dependence of accretion and disk evolution is critical to constrain the planet formation phase and identify the disk clearing mechanisms (e.g., Alexander & Armitage 2006; Rosotti et al. 2017). Population-wide surveys of disk-bearing versus accreting YSOs in open clusters as a function of age have suggested that circumstellar disks tend to disperse within 5–10 Myr (e.g., Hernández et al. 2007; Bell et al. 2013; Ribas et al. 2014), and that the fraction of accreting cluster members declines with age on similar or shorter timescales (e.g., Fedele et al. 2010; Briceño et al. 2019; Flaccomio et al. 2023). However, this global picture is affected by local differences between individual clusters, such as the



Original content from this work may be used under the terms of the [Creative Commons Attribution 4.0 licence](https://creativecommons.org/licenses/by/4.0/). Any further distribution of this work must maintain attribution to the author(s) and the title of the work, journal citation and DOI.

specific mass spectrum of member stars and the external radiation field, which can impact the disk lifetimes (e.g., Guarcello et al. 2010; Ribas et al. 2015; Coleman & Haworth 2022). In addition, a different sensitivity in accretion and disk diagnostics may bias the comparison on the respective evolutionary timescales because young stars can still be accreting even after the dust content of the inner disk has been cleared (Thanathibodee et al. 2022).

Wide-field multiband photometric surveys provide the most efficient approach for a uniform mapping of the disk and accretion properties in large samples of YSOs. Thermal emission from circumstellar dust is responsible for the distinctive infrared (IR) flux excess in the spectral energy distribution (SED) of disk-bearing YSOs (e.g., Robitaille et al. 2007), and tracing how this excess emission varies with wavelength provides a direct proxy for the disk evolutionary stage (e.g., Lada 1987; Evans et al. 2009). Mass accretion onto the star can be studied by measuring the flux excess at short wavelengths ( $<400$  nm) emitted by the surface shocks that develop where material is deposited from the accretion column (e.g., Calvet & Gullbring 1998; Orlando et al. 2010; Matsakos et al. 2013). Photometric observations in the ultraviolet (UV) provide a robust tracer of the total accretion luminosity on individual sources (e.g., Gullbring et al. 1998; Rigliaco et al. 2011; Manara et al. 2012; Venuti et al. 2014). Accretion activity is also commonly quantified by measuring the intensity of the hydrogen emission lines (most prominently  $H\alpha$ ) produced by the heated and accelerated gas in the accretion columns (e.g., White & Basri 2003; Kurosawa et al. 2006; Alcalá et al. 2017), which can be captured photometrically by adopting narrowband  $H\alpha$  filters (e.g., De Marchi et al. 2010; Barentsen et al. 2011). For both accretion diagnostics, simultaneous color information in optical broadband filters is crucial for a reliable evaluation of stellar parameters, photospheric flux, and chromospheric emission (e.g., Manara et al. 2013).

In this paper, we explore the impact of stellar mass and environmental conditions on the properties of accretion disks in YSOs by focusing on the Lagoon Nebula region. With a typical age of  $<1$  Myr at its core (the NGC 6530 cluster; Prisinzano et al. 2019), a rich population of a few thousand members (Feigelson et al. 2013; L. Rebull et al. 2024, in preparation), and several dozen massive O/B stars (Tothill et al. 2008; Povich et al. 2017), this region is an ideal target for studying how these factors may disrupt the dynamics of accretion and disk evolution. The Lagoon Nebula has been the object of numerous investigations across the wavelength spectrum, including recent studies on the reddening law and age spread in the region (Prisinzano et al. 2019), on the spatial structure and dynamical formation history of the NGC 6530 cluster (Damiani et al. 2019), and on the instantaneous accretion properties of its solar-to-subsolar mass members (Kalari et al. 2015). Variability studies of Lagoon Nebula YSOs (e.g., Venuti et al. 2021; Ordenes-Huanca et al. 2022) have shown that many cluster members are actively interacting with their circumstellar disks. Notably, the Lagoon Nebula was one of the few young stellar fields to be encompassed by the Kepler/K2 mission (Howell et al. 2014), resulting in a uniquely detailed description of the diverse variability patterns that can be found among YSOs (e.g., Cody et al. 2014; Cody & Hillenbrand 2018) and how they relate to the specific accretion

and star-disk interaction dynamics in the final stages of stellar mass assembly (e.g., Fischer et al. 2022).

In Venuti et al. (2021), we presented a comprehensive study of variability behaviors and timescales for YSOs in the Lagoon Nebula by leveraging the Kepler/K2 light curves and simultaneous multicolor time-series photometry obtained from the ground in the  $u$ ,  $g$ ,  $r$ ,  $i$ ,  $H\alpha$  filters. Their study revealed clear mass-dependent trends in the occurrence of different light-curve patterns, categorized in amplitude and shape according to their degree of periodicity and symmetry, as defined by Cody et al. (2014). In this paper, we take advantage of the full area coverage provided by the  $u$ ,  $g$ ,  $r$ ,  $i$ ,  $H\alpha$  data set to characterize accretion and disk properties for Lagoon Nebula YSOs across a wider region around the K2 field, and to investigate how these properties evolve as a function of stellar parameters and local conditions. This work extends the results of previous snapshot investigations by providing a detailed view of how star-disk characteristics within the region change throughout the time domain from timescales of hours to years. We also explore the connection between accretion and disk evolution, drawing a homogeneous picture over the entire spatial extent of the Lagoon Nebula and in a sweeping range in stellar masses ( $\sim 0.2$ – $5 M_{\odot}$ ).

The paper is organized as follows. Section 2 details the photometry acquisition procedures for our data sets. Section 3 details the selection of Lagoon Nebula members and their disk classifications. Section 4 discusses the derivation of fundamental stellar parameters. Section 5 reports how accreting stars were identified based on UV and  $H\alpha$  emission. Section 6 explores the connection between accretion and stellar mass, the simultaneity of accretion signatures at different wavelengths, and the variability of accretion on different timescales. In Section 7, we discuss the implications of our findings for the pattern of disk evolution as a function of stellar mass and spatial location. Section 8 summarizes our conclusions and future perspectives.

## 2. Observations and Data Processing

Our work is built on multiband light curves obtained for young stars in the Lagoon Nebula with the OmegaCAM wide-field imager (Kuijken et al. 2002; Kuijken 2011) at the VLT Survey Telescope (VST; Arnaboldi et al. 1998). This observing campaign, described in Venuti et al. (2021), complemented the Kepler/K2 monitoring of the NGC 6530 cluster during K2 Campaign 9. In Section 2.1, we summarize the technical details and light-curve extraction procedure relevant to these two primary data sets, while ancillary data sets that were used to classify the evolutionary status of our target population are briefly described in Section 2.2.

### 2.1. Primary Data Sets: VST/OmegaCAM and Kepler/K2

The VST/OmegaCAM observations were conducted between 2016 June 16 and July 10 under program 297.C-5033(A). A thorough description of this observing run and of the associated data reduction and photometry extraction procedures was provided in Section 2.3 of Venuti et al. (2021). Here, we summarize the key information pertaining to this data set.

By adopting a dithered observing pattern with a sequence of two short and two long exposures for each single observing block, VST/OmegaCAM provided a five-band ( $u$ ,  $g$ ,  $r$ ,  $i$ ,  $H\alpha$ )

map of an area of approximately  $1^{\circ}3 \times 1^{\circ}2$  around (R. A., decl.)  $\sim(271.0, -24.36)$ . Each star imaged with VST/OmegaCAM was observed at least 6 (and generally 17) times at a typical cadence of one visit per day over 14 nonconsecutive days during the monitored period. Object fluxes were measured via the Cambridge Astronomy Survey Unit (CASU) pipeline<sup>12</sup> and were then transformed into magnitudes and calibrated to the Sloan Digital Sky Survey (SDSS) system (Fukugita et al. 1996) by taking as reference the catalog of the VST Photometric H $\alpha$  Survey of the Southern Galactic Plane and Bulge (VPHAS+; Drew et al. 2014), which employed the same instrument and filter set.

As explained in detail in Section 3.1, a cross-correlation of our VST/OmegaCAM catalog with a literature census of Lagoon Nebula YSOs yielded a list of 1012 members for which photometric measurements are available in our data set. For 415 of these, we could also extract high-precision time-series photometry from K2 Campaign 9. This subset represents an extension of the sample presented in Venuti et al. (2021) owing to an expanded membership search (Section 3.1) and to the implementation of additional light-curve extraction techniques that allowed us to enlarge the brightness range of K2 targets, as detailed below.

The K2 observations were limited to an area of  $\sim 0^{\circ}26 \times 0^{\circ}15$  at the heart of the Lagoon Nebula (where NGC 6530 is located). For all stars in the K2 sample, we created both aperture and point-spread function (PSF) light curves. Aperture photometry for the bulk of objects was carried out as described in Venuti et al. (2021); for targets that were saturated on the detector, we instead employed irregularly shaped aperture masks with the `lightkurve` Python package (Lightkurve Collaboration et al. 2018). The extent of these apertures was selected manually based on the stellar flux distribution and on the location of saturation spikes.

Photometry for the faintest sources in the K2 frames benefited from a PSF fitting approach, which was carried out with the `Photutils` Python package. An effective point-spread function (ePSF) was built based on the combined flux data of eight stars from all 3284 K2 Lagoon superstamp images. These eight stars were selected based on criteria of brightness (Kepler magnitude range  $\sim 10$ – $15$ ) and lack of neighbors (no sources of similar brightness within several pixels).

The stellar data, including sky positions, for the stars we used to create the ePSF were extracted from the Gaia archive (Gaia Collaboration et al. 2016, 2023). The same ePSF model was then used for the flux fitting for each star in each K2 frame. The centroids were fixed based on each image world coordinate system (WCS) and the known star positions.

For circular aperture and PSF-based light curves, we found that the measured flux was sensitive to the object centroid position. This jitter is a well-known phenomenon for K2 time-series photometry, and it can be mitigated by estimating and removing position-correlated flux trends. We carried out this process with the `k2sc` package (Aigrain et al. 2016). `k2sc` employs a Gaussian process model to estimate any underlying stellar variability in addition to flux changes caused by intrapixel sensitivity variations. Upon applying this detrending method, light curves were output with decreased systematic effects.

The final K2 light curves were chosen among the available versions based on which displayed the lowest noise levels, and consequently, the clearest variability signature. Preference to PSF or photometry with the smallest apertures was given when companion sources were present within 1–2 pixels ( $4''$ – $8''$ ).

## 2.2. Auxiliary Data Sets

In order to classify YSOs in our sample as a function of their disk evolutionary stage, we employed near- to mid-IR photometry from three archival databases: the Two Micron All Sky Survey (2MASS; Skrutskie et al. 2006), the Spitzer/InfraRed Array Camera (IRAC; Fazio et al. 2004), and the Wide-field Infrared Survey Explorer (WISE; Wright et al. 2010). The details regarding the literature sources that were merged to assemble this IR compilation are provided in Venuti et al. (2021). The 2MASS and the IRAC catalogs both extend over the entire  $\sim 0.9$  sq. deg. area over which the Lagoon Nebula population is distributed; the IRAC coverage in volume of sources is  $\sim 10\%$  less complete than the 2MASS coverage. On the other hand, the WISE coverage is only about 15% complete with respect to 2MASS, and the central regions of the Lagoon Nebula, where the majority of YSOs are located, are especially undersampled.

## 3. Target Population

### 3.1. Sample Selection and Cluster Membership

To identify all young stars in the VST/OmegaCAM field, we conducted a comprehensive literature search of all potential YSO members reported for the Lagoon Nebula region in the wavelength spectrum (Venuti et al. 2021, Section 2.1; L. Rebull et al. 2024, in preparation). We then cross-matched the resulting list with the complete catalog of point sources extracted from the VST/OmegaCAM observations. This procedure led to a selection of 415 confirmed or possible Lagoon Nebula members with a counterpart in the K2 mosaic and another 597 without K2 light curves, but with a VST/OmegaCAM detection in at least the  $g$ ,  $r$ ,  $i$  filters to enable stellar parameter (extinction, “ $A_V$ ,” spectral type, “SpT”) estimation following the approach of Venuti et al. (2021).

Our final YSO sample is introduced in Table 1. Overall, a complete  $u$ ,  $g$ ,  $r$ ,  $i$ , H $\alpha$  photometric set is available for 486 of the 1012 objects (48.0%). This is due to the fact that the completeness level of our  $u$ -band catalog drops quickly on the fainter side of  $r \sim 16$ , which corresponds to the average  $r$ -band magnitude of our target list. Another 462 of the 1012 YSOs in our sample (45.7%) lack  $u$ -band photometry, but have  $g$ ,  $r$ ,  $i$ , H $\alpha$  photometry. Hence, at least one accretion indicator ( $u$ -band excess and/or H $\alpha$  emission, as discussed in Section 5) is available for 97% of our sample. The derived variability classes from the K2 light curves, when available, are also provided in Table 1; they are used in Section 6 to investigate the connection between photometric variability signatures and the dynamics and intensity of disk accretion activity.

In order to assess the membership status of stars in our sample, we reviewed the membership criteria available in the literature, which fall broadly into three categories:

1. Photometric, which encompasses all emission properties indicative of a YSO nature, including X-ray detection, UV excess, IR excess, shape of the SED, and H $\alpha$  emission (membership data from Sung et al. 2000; Rauw

<sup>12</sup> <http://casu.ast.cam.ac.uk/surveys-projects/vst>

**Table 1**

List of Lagoon Nebula Members Included in This Study, with Corresponding Coordinates, Derived Membership Flag, Disk Classification, Accretion Status, K2 Variability Class (when Available), VST/OmegaCAM  $u$ ,  $g$ ,  $r$ ,  $i$ , H $\alpha$  Photometry, and Derived Stellar and Accretion Parameters

Identifier <sup>a</sup>	R.A. (deg.)	Decl. (deg.)	Mem.	Disk <sup>b</sup>	Acc. <sup>c</sup>	K2 <sup>d</sup>	$u$ (mag)	$g$ (mag)	$r$ (mag)	$i$ (mag)	H $\alpha$ (mag)	SpT	$A_V$ (mag)	$L_{\text{bol}}$ ( $L_{\odot}$ )	$M_{\star}$ ( $M_{\odot}$ )	$R_{\star}$ ( $R_{\odot}$ )	$\log t$ (yr)	$\log \dot{M}_{\text{acc}}$ ( $M_{\odot} \text{ yr}^{-1}$ )	$\Delta \dot{M}_{+}^e$ (dex)	$\Delta \dot{M}_{-}^f$ (dex)
224290871	270.9510	−24.5109	?	y*	0	QPS	18.48	16.54	15.17	14.49	14.93	K8.3	0.04	2.35	0.53	3.23	5.43	...	...	...
224297601	271.0980	−24.4987	y	n*	0	P	20.08	17.86	16.42	15.73	16.06	K7	0.47	0.91	0.75	1.86	6.17	...	...	...
224305947	271.1103	−24.4834	y	y	0	QPD	19.44	17.06	15.49	14.77	15.16	K7.3	1.15	3.93	0.61	3.93	5.15	...	...	...
224308921	271.0940	−24.4781	y	y*	1	QPS	16.31	15.10	14.48	14.16	14.35	F5.3	1.02	4.87	1.38	1.73	7.14	−8.28	0.26	...
224311070	270.9652	−24.4740	y	y	1	APD	16.88	15.40	14.49	14.07	14.17	G6	1.11	5.30	1.93	2.51	6.57	−8.08	0.22	0.72
224311432	271.1643	−24.4734	?	n	1	N	15.81	14.59	13.93	13.64	13.67	G4.5	0.34	4.72	1.80	2.30	6.69	−8.27	0.46	0.28
224311447	271.1992	−24.4733	y	n	0	MP	11.56	11.27	11.26	11.26	11.21	A1.5	0.37	79.5	2.76	3.51	6.42	...	...	...
224312151	271.0848	−24.4721	y	n	2	QPS	17.76	15.71	14.36	13.77	13.91	K7	0.25	5.11	0.63	4.42	...	−7.40	0.19	0.16
224313065	271.1710	−24.4704	?	n	1	N	15.50	14.39	13.91	13.72	13.77	G1.3	0.22	4.46	1.61	2.10	6.86	−8.10	0.16	0.17
224314197	270.8580	−24.4683	y	n	0	P	18.33	16.43	15.40	14.99	15.18	K3.5	0.31	1.55	1.23	1.94	6.37	...	...	...

**Notes.** A full version of this table is provided in electronic format. A portion is shown here for guidance regarding its form and content.

<sup>a</sup> Cross-identification number from one of the following catalogs: Ecliptic Plane Input Catalog (EPIC; Huber et al. 2016; Sung et al. 2000; SCB; Prisinzano et al. 2005; WFI; 2MASS; VPHAS+; GES).

<sup>b</sup> Disk classification as y (high-confidence disk-bearing), y\* (disk-bearing with a more uncertain classification), n (high-confidence disk-free), n\* (disk-free with a more uncertain classification), and ? (disk candidate).

<sup>c</sup> Accreting status classification as 1 (accreting), 2 (potential accretor), and 0 (nonaccreting).

<sup>d</sup> See Venuti et al. (2021); possible values include P (periodic), QPS (quasi-periodic symmetric), S (stochastic), B (burst), QPD (quasi-periodic dipper), APD (aperiodic dipper), N (flat-line), and U (unclassifiable).

<sup>e</sup> Logarithmic amplitude of  $\dot{M}_{\text{acc}}$  variations above the typical (median)  $\dot{M}_{\text{acc}}$  value measured during the monitored period.

<sup>f</sup> Logarithmic amplitude of  $\dot{M}_{\text{acc}}$  variations below the typical (median)  $\dot{M}_{\text{acc}}$  value measured during the monitored period. This parameter is only provided for objects that showed detectable  $\dot{M}_{\text{acc}}$  levels at all epochs during our monitoring campaign.

(This table is available in its entirety in machine-readable form.)



- et al. 2002; Damiani et al. 2004; Kumar & Anandarao 2010; Broos et al. 2013; Castro 2013; Povich et al. 2013; Kalari et al. 2015).
- 2. Kinematic, which encompasses kinematic or astrometric evidence of belonging to the cluster from radial velocity, proper motion, and/or parallax data (van den Ancker et al. 1997; Chen et al. 2007; Prisinzano et al. 2007; Damiani et al. 2019).
- 3. Spectroscopic, i.e., Li absorption in the stellar spectrum (Arias et al. 2007; Prisinzano et al. 2007).

For each object in our list, we flagged the membership according to individual criteria, and then assigned a final classification to our stars as either bona fide members or candidate members. Bona fide members were selected as objects displaying Li absorption indicative of youth, satisfying at least one membership criterion from two different categories, or two distinct membership criteria from a single category. Candidate members were defined as objects without a recorded Li absorption measurement and satisfying only one criterion for membership, or with a member status originating from a single literature study. The results from this classification are reported in Table 1; 787 of the 1012 stars were classified as bona fide members (78%), and the remaining 225 were classified as candidate members.

### 3.2. Disk Classification

As mentioned in Section 2.2, the available optical photometry was combined with literature IR photometric catalogs to classify the evolutionary status of individual YSOs with respect to their disk properties. The same multi-indicator classification procedure as outlined in Venuti et al. (2021) was uniformly extended to the complete sample of 1012 stars considered here. In summary, the criteria considered for the disk classification included

- i. the  $\alpha_{\text{IRAC}}$  index defined at  $[3.6] - [8.0]$  wavelengths (Teixeira et al. 2012);
- ii. the location of individual stars in near-IR (2MASS  $J, H, K$ ) and mid-IR (WISE W1, W2, W3) color-color diagrams with respect to the loci of disk-bearing stars (Meyer et al. 1997; Koenig & Leisawitz 2014);
- iii. the reddening-free optical-IR indices  $Q_{JHHK}$  and  $Q_{VIJK}$  (Damiani et al. 2006).

The disk flags from the various disk indicators were then merged to assign a final disk class to each target. In case of a consistent disk classification for a given source across all indicators, the corresponding class was assigned as the final disk class. In case of discordant information from different indicators, we adopted the following approach:

- 1. in the case of a disk detection at mid-IR wavelengths but not at near-IR wavelengths, the target was classified as disk-bearing, as it may be hosting a more evolved disk that is no longer traceable in the near-IR;
- 2. in the case of a disk detection at near-IR wavelengths but not at mid-IR wavelengths, the target was classified as a disk candidate object when the mid-IR flux measurements were still consistent with the disk-bearing color loci within the photometric uncertainties, and as disk-free otherwise;

- 3. in the case of a disk candidate flag in the mid-IR and a disk nondetection in the near-IR, the object was retained as a disk candidate;
- 4. in the case of a disk nondetection in the mid-IR and a disk candidate flag in the near-IR, the object was classified as disk-free.

This procedure enabled assignment of a disk class to 844 of the 1012 objects. Of these, 229 (27.1%) were classified as disk-bearing, 568 (67.3%) were classified as disk-free, and 47 (5.6%) were classified as disk candidate objects. For stars classified as either disk-bearing or disk-free, we also introduced a further flag aimed at qualifying the strength of the disk status classification. For disk-free stars, we attributed a strong classification (high-confidence) flag to sources for which at least two distinct disk indicators in separate IR band sets were available, with all providing a coherent no-disk classification. For disk-bearing stars, we attributed a strong classification flag to sources that satisfied one of the following criteria: i)  $\alpha_{\text{IRAC}} > -1.8$ , corresponding to a thick-disk classification; ii) availability of disk indicators in all three band sets and definite disk-bearing status according to at least two of them; iii) availability of disk indicators in two separate band sets and classification incompatible with disk-free status at all available bandpasses; and iv) availability of multiple disk indicators in a given band set (namely  $J, H, K$ ) and definite disk-bearing classification from all indicators. This additional flagging system resulted in an assignment of  $\sim 73\%$  of the disk-free stars and  $\sim 64\%$  of the disk-bearing stars with a strong classification label, while sources that did not satisfy the listed criteria were considered more uncertain disk-bearing or disk-free classifications. The results from this classification are reported in Table 1.

To derive a statistical estimate of the true disk fraction in our sample, which accounts for objects that lack any disk status information, we explored a grid of theoretical disk fractions extending over the entire range of possible values with a step of 0.01, and for each step of the grid, we simulated a population of 1012 stars with an injected disk fraction corresponding to the grid value. We then extracted 844 members from the simulated sample of 1012 and determined for how many of these a disk-bearing status had been assigned. For each injected disk fraction, we repeated this procedure 10,000 times, and out of these 10,000 iterations, we tallied the instances for which the number of “observed” stars with disk-bearing status, extracted from the total simulated sample was consistent with the real observations (i.e., comprised between a minimum dictated by the number of stars classified as disk-bearing with high confidence in our sample and a maximum dictated by the sum of disk-bearing and disk candidate objects, plus low-confidence disk-free objects). We then built a distribution of the resulting tallies as a function of the assumed disk fraction and fit its profile with a Gaussian distribution, whose mean and standard deviation provided us with a best statistical disk fraction  $f_{\text{disk}}$ , estimated to be  $0.34 \pm 0.14$  in our entire sample. When this statistical analysis was restricted to bona fide members alone, a similar  $f_{\text{disk}} = 0.37 \pm 0.16$  was derived.

## 4. Stellar Properties

In this section, we describe how stellar parameters were estimated from our collection of multiband photometry. We start with individual  $A_V$ -SpT values (Section 4.1), which are

**Table 2**

Typical Uncertainties on the Stellar and Accretion Parameters Derived Here as a Function of Spectral Class

SpT	$\sigma_{T_{\text{eff}}}$ ( $T_{\text{eff}}$ )	$\sigma_{BC_V}$ (mag)	$\sigma_{M_{\text{bol}}}$ (mag)	$\sigma_{L_{\text{bol}}}$ ( $L_{\text{bol}}$ )	$\sigma_{M_*}$ ( $M_*$ )	$\sigma_{R_*}$ ( $R_*$ )	$\sigma_{\log \dot{M}}$ (dex)
O	0.020	0.25	0.40	0.37	...	0.19	...
B	0.085	0.15	0.34	0.32	0.11–0.14	0.23	0.34
A	0.015	0.14	0.34	0.31	0.10–0.12	0.16	0.34
F	0.020	0.08	0.32	0.29	0.11–0.13	0.15	0.34
G	0.035	0.09	0.32	0.30	0.16–0.18	0.17	0.36
K	0.050	0.08	0.32	0.29	0.25–0.32	0.18	0.38
M	0.030	0.26	0.40	0.37	0.18–0.23	0.19	0.38

**Note.** The typical estimates provided for  $\sigma_{T_{\text{eff}}}$ ,  $\sigma_{L_{\text{bol}}}$ ,  $\sigma_{M_*}$ , and  $\sigma_{R_*}$  are fractional uncertainties. No typical  $\sigma_{M_*}$  range and  $\sigma_{\log \dot{M}}$  are reported for O-type stars because no  $M_*$  estimates could be derived for them following the method outlined in the text.

required, together with suitable effective temperature ( $T_{\text{eff}}$ ; Section 4.2) and bolometric correction (BC; Section 4.3) scales, to derive the bolometric luminosities ( $L_{\text{bol}}$ ; Section 4.4). We then build the Hertzsprung–Russell (HR) diagram of the cluster and estimate stellar masses, ages, and radii (Section 4.5). All parameters obtained for each star are reported in Table 1, and the associated uncertainties are listed as a function of spectral class in Table 2. In turn, the derived stellar parameters are key to calculating mass accretion rates, as presented later in Section 6.1.

#### 4.1. Individual Extinctions and Spectral Types

Estimates of SpT were derived for our targets following the procedure described in Venuti et al. (2021; see their Figure 3 for an illustration of the method). In a nutshell, the observed colors of each star in the ( $r-i$ ,  $g-r$ ) diagram were compared to the unreddened reference SpT–color sequence tabulated in VST/OmegaCAM filters by Drew et al. (2014). For each spectral subclass, we calculated the required color corrections (i.e.,  $A(g-r)$  and  $A(r-i)$ ) to be applied to our observed colors in order to match the expected colors for that SpT, assuming the anomalous reddening law reported by Prisinzano et al. (2019). We then selected the SpT estimate that corresponded to the best agreement between the calculated  $A(g-r)$  and  $A(r-i)$  and defined our best  $A_V$  as the average between the derived color-dependent extinction coefficients.

In order to strengthen the SpT determination, we also applied the same procedure to the ( $V-I$ ,  $B-V$ ) diagram built from literature photometry, using the reference sequence of unreddened colors tabulated by Pecaut & Mamajek (2013). Although potentially affected by larger uncertainties due to data inhomogeneity and nonsimultaneity, the latter diagram benefited our  $A_V$ –SpT derivation procedure by mitigating the impact of degenerate trends between the ( $r-i$ ,  $g-r$ ) color sequence and the adopted reddening law that prevented accurate SpT determinations for some objects, as reported in Venuti et al. (2021). The individual solutions from each diagram were then merged as follows:

1. when the best solutions from both diagrams were consistent within half a spectral class, an averaged solution was adopted as best  $A_V$ –SpT parameters;

2. when multiple valid solutions emerged from one or both diagrams, we selected the solution that provided the best agreement between the two sets of results;
3. when no converging solution could be found, and in the absence of literature information suggesting otherwise, we favored the result extracted from  $g$ ,  $r$ ,  $i$  colors, owing to their simultaneity and widespread availability in our sample of Lagoon Nebula members (while  $B$ ,  $V$ ,  $I$  colors are only available for 63% of our targets).

At the end of this procedure, we were able to assign an SpT estimate to 966 of the 1012 (95%) stars in our sample, about 51% of which had individual SpT estimates from both sets of  $g$ ,  $r$ ,  $i$  and  $B$ ,  $V$ ,  $I$  colors. The resulting spectral class distribution in our sample is as follows:

1. O-type stars: 0.7%
2. B-type stars: 4.6%
3. A-type stars: 8.0%
4. F-type stars: 11.6%
5. G-type stars: 14.2%
6. K-type stars: 50.4%
7. M-type stars: 10.5%

#### 4.2. Effective Temperatures ( $T_{\text{eff}}$ )

The derived SpT were converted into  $T_{\text{eff}}$  following a literature reference scale. Multiple published SpT– $T_{\text{eff}}$  scales were compared and their class-by-class difference evaluated to estimate the uncertainty resulting from this conversion on the SpT-dependent  $T_{\text{eff}}$  values. More specifically, we considered the following scales:

1. Böhm-Vitense (1981), Pecaut & Mamajek (2013), and Gray & Corbally (2009) for O-type stars;
2. Böhm-Vitense (1981), Gray & Corbally (2009), Pecaut & Mamajek (2013), and Kenyon & Hartmann (1995) for B-type stars;
3. Gray & Corbally (2009), Pecaut & Mamajek (2013), and Kenyon & Hartmann (1995) for A-type stars;
4. Gray & Corbally (2009), Pecaut & Mamajek (2013), Herczeg & Hillenbrand (2014), and Kenyon & Hartmann (1995) for F/G/K stars;
5. Gray & Corbally (2009), Pecaut & Mamajek (2013), Herczeg & Hillenbrand (2014), and Luhman et al. (2003) for M-type stars.

For each compilation and spectral subclass, we calculated the absolute difference in tabulated  $T_{\text{eff}}$  with respect to the Gray & Corbally (2009) scale, which provides the most extensive SpT coverage. The largest percentage discrepancy measured across all scales for each subclass was then selected, and the final fractional uncertainty on  $T_{\text{eff}}$  was defined class by class from the median percentage error in all relevant subclasses, rounded to the closest multiple of 0.5%. These uncertainties are reported in Table 2, while individual  $T_{\text{eff}}$  values were assigned using the Gray & Corbally (2009) SpT– $T_{\text{eff}}$  scale.

Independent spectroscopically determined  $T_{\text{eff}}$  values were obtained for  $\sim 34\%$  of our sample within the Gaia-ESO Survey (GES; Gilmore et al. 2012; Randich et al. 2013), as published in Prisinzano et al. (2019). A comparison between our adopted  $T_{\text{eff}}$  values and the GES parameters revealed that the vast majority (90%) of objects in common have consistent  $T_{\text{eff}}$  estimates within a factor  $\sim 1.2$ , corresponding to a range of 1–3

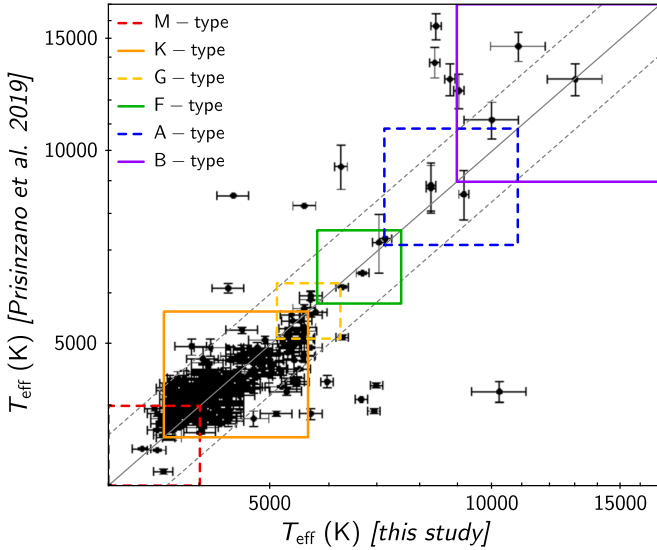


**Figure 1.** Comparison between  $T_{\text{eff}}$  estimates derived in this study as presented in Section 4.2 and the values obtained in Prisinzano et al. (2019) for objects in common between the two samples. The solid gray line traces the equality line on the diagram, while the dotted gray lines trace a difference between the two  $T_{\text{eff}}$  sets that amounts to a factor of 1.2. The colored boxes mark the ranges in  $T_{\text{eff}}$  associated with different spectral classes, as labeled in the legend. The overlapping corners between adjacent boxes correspond to the transition between the ninth subclass of the previous spectral group and the zeroth subclass of the following spectral group, while the delimiting  $T_{\text{eff}}$  values take the uncertainties listed in Table 2 into account.

spectral subclasses at both the lower- (G/K stars) and higher-mass end (A stars), as illustrated in Figure 1, and only  $\sim 4\%$  of the objects appear to be significant outliers with inconsistent spectral classes assigned from the two analyses. Disk-bearing and disk-free stars exhibit a similar distribution in the diagram, with median measured ratios between our  $T_{\text{eff}}$  values and the estimates of Prisinzano et al. (2019) that amount to 1.00 and 0.98, respectively. The interquartile range measured around the central value for disk-bearing stars (0.13) is slightly larger than that measured for disk-free stars (0.10), possibly reflecting an additional source of scatter associated with some residual contribution of disk-related phenomena to the optical stellar colors. Nevertheless, the overall consistency in stellar properties between disk-bearing and disk-free stars that we observe at  $g$ ,  $r$ ,  $i$  wavelengths indicates that while this effect may reduce the accuracy of individual parameters derived for some stars with enhanced disk activity, it would not impact the statistical inferences that we draw from our analysis.

#### 4.3. Bolometric Corrections

To convert our apparent magnitudes into bolometric magnitudes, we compiled a  $T_{\text{eff}}$ -dependent  $V$ -band BC ( $BC_V$ ) scale with uncertainties by comparing the individual scales published by Schmidt-Kaler (1982), Bessell et al. (1998), Pecaut & Mamajek (2013), and Kenyon & Hartmann (1995). To derive a functional form that would link the values of  $T_{\text{eff}}$  and  $BC_V$ , we conducted a polynomial fit to each scale. We then compared the predictions between each pair of scales over the most restrictive  $T_{\text{eff}}$  range covered by both and measured the absolute difference in predicted  $BC_V$  values as a function of  $T_{\text{eff}}$ . We used the  $T_{\text{eff}}$ -SpT scale from Gray & Corbally (2009) to separate the  $T_{\text{eff}}$  grid into spectral classes, and for each spectral class and pair of conversion scales, we derived the

typical uncertainty on  $BC_V$  as the median discrepancy in the predicted values at a given temperature for the entire spectral class. We then defined the class-by-class uncertainty on  $BC_V$  as the median difference calculated for each spectral class for all pairs of conversion scales. The resulting uncertainties on  $BC_V$  are listed in Table 2. Our adopted  $BC_V$  values were extracted from Schmidt-Kaler (1982), because they provide the most comprehensive coverage in spectral types of the references considered here.

#### 4.4. Bolometric Magnitudes and Luminosities

In order to apply the  $BC_V$  scale to optical magnitudes in our sample, we used the transformation relations by Jester et al. (2005) and Jordi et al. (2006) to convert the VST/OmegaCAM measurements into Johnson-Cousins  $V$ -band magnitudes. Both transformations use the observed  $g$ -band magnitudes and  $g-r$  colors and yield consistent results within  $\sim 0.009$  mag. On the other hand, the typical absolute difference between converted and archival  $V$ -band magnitudes (when available) in our sample ranges from  $\sim 0.03$  mag at  $V \sim 11.2$  to  $\sim 0.09$  mag at  $V \sim 18.8$ , which encompasses 90% of the population over which this comparison could be performed. We then assumed the median value  $\sim 0.06$  mag as the uncertainty on the derived  $V$ -band magnitudes, averaged from the two sets of transformations. Absolute magnitudes  $M_V$  were then derived as  $V - A_V - 5 \cdot (\log d - 1)$ , with an adopted distance  $d$  of  $1325 \pm 113$  pc (Damiani et al. 2019).  $T_{\text{eff}}$ -dependent  $BC_V$  values were added to the calculated  $M_V$  to derive the bolometric magnitudes  $M_{\text{bol}}$ , and the bolometric luminosities  $L_{\text{bol}}/L_{\odot}$  were estimated as  $10^{0.4 \cdot (M_{\text{bol}, \odot} - M_{\text{bol}})}$ .

To account for the uncertainties discussed earlier, we estimated the following typical parameter errors:

1.  $\sigma_{M_V} = \sqrt{\sigma_V^2 + \sigma_{A_V}^2 + \left[ \left( \frac{5}{d \ln 10} \right) \sigma_d \right]^2} \simeq 0.31$ , following from the aforementioned uncertainties on  $V^{13}$  and  $d$ , and from the typical total uncertainty on the adopted value of  $A_V$ ;
2.  $\sigma_{M_{\text{bol}}} = \sqrt{\sigma_{M_V}^2 + \sigma_{BC_V}^2}$ , dependent on spectral class, as listed in Table 2;
3.  $\frac{\sigma_{L_{\text{bol}}}}{L_{\text{bol}}} = 0.4 \cdot \ln 10 \cdot \sigma_{M_{\text{bol}}}$ , also dependent on spectral class, as reported in Table 2.

#### 4.5. Stellar Masses ( $M_{\star}$ ), Ages ( $t$ ), and Radii ( $R_{\star}$ )

The derived values of  $T_{\text{eff}}$  and  $L_{\text{bol}}$  were used to build the HR diagram of the region, illustrated in Figure 2.

David et al. (2019) presented a thorough comparative assessment of different pre-main-sequence evolutionary model grids with regard to the determination of intrinsic stellar parameters. Based on their analysis, we adopted the Modules for Experiments in Stellar Astrophysics (MESA) Isochrones and Stellar Tracks (MIST) models (Choi et al. 2016; Dotter 2016) without rotation and with solar metallicity to interpolate the position of our targets in the HR diagram and to estimate individual masses ( $M_{\star}$ ) and ages ( $t$ ). For each object, we extracted the  $(\log T_{\text{eff}}, \log L_{\text{bol}})$  coordinates of the delimiting points from the two closest isochrones and mass tracks around

<sup>13</sup> We note that assuming a magnitude-dependent  $\sigma_V$ , as opposed to the uniform value discussed earlier in the text, would only lead to a modest ( $\sim 2\%$ ) change in the derived  $\sigma_{M_V}$  with respect to the typical estimate listed here.



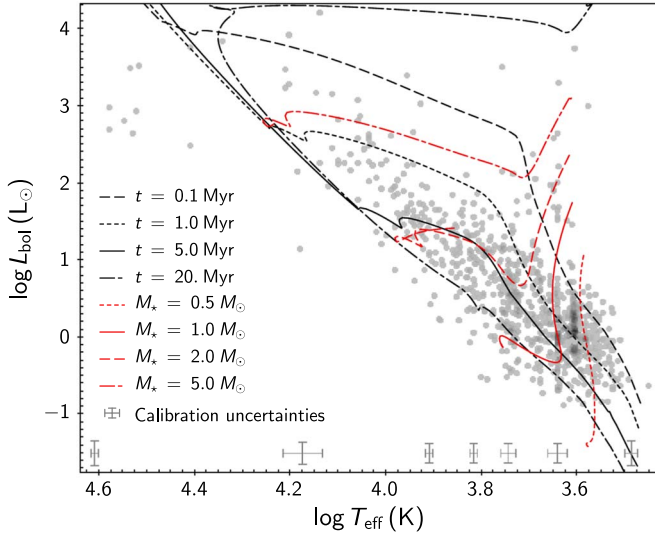


**Figure 2.** Distribution of Lagoon Nebula members in the HR diagram. The model mass tracks (red) and isochrones (black) shown on the diagram were extracted from the MIST compilation (Choi et al. 2016; Dotter 2016), assuming solar metallicity and without rotation effects. The error bars at the bottom illustrate the SpT-dependent typical uncertainties on  $T_{\text{eff}}$  and  $L_{\text{bol}}$  values, as discussed in Sections 4.2 and 4.4.

its position, and conducted a linear interpolation over  $\log L_{\text{bol}}$  and  $\log T_{\text{eff}}$  to extract the best-fit  $t$  and  $M_*$  values. The corresponding  $M_*$  uncertainty ( $\sigma_{M_*}$ ) was then estimated by drawing a  $[\pm\sigma_{T_{\text{eff}}}, \pm\sigma_{L_{\text{bol}}}]$  box around the data point in the diagram, and determining the limiting  $M_*$  values from the range of isochrones that intersected the boxed area. The resulting typical  $\sigma_{M_*}$  ranges are listed as a function of SpT in Table 2.

Overall, an estimate of  $M_*$  was obtained for 924 of the 1012 targets in our sample (91%); 40 of the remaining 88 objects have no ( $L_{\text{bol}}$ ,  $T_{\text{eff}}$ ) derivations for a placement in the HR diagram, 43 appear to be located below the main-sequence turnoff in Figure 2, and 5 appear to be located above the pre-main-sequence onset (i.e., brighter than predicted for the earliest ages at the corresponding  $T_{\text{eff}}$ ) in the diagram. Disk-bearing stars appear to be over-represented among the sources without an  $M_*$  estimate (29 versus 30 disk-free stars, although disk-free stars are 2.5 times as frequent as disk-bearing stars in our sample, as discussed in Section 3.2). In both groups, the subsets of objects without  $M_*$  are about evenly split between cases lacking ( $L_{\text{bol}}$ ,  $T_{\text{eff}}$ ) estimates and cases for which no isochrone-fitting solution could be extracted due to their position in the HR diagram. However, only about one-third of the disk-free cases without an isochrone-fitting solution have a strong no-disk classification, which suggests that the apparent properties of HR diagram outliers with respect to the pre-main-sequence model grid may be linked to some contamination by disk-related phenomena.

The mass distribution derived for our sample is illustrated in Figure 3. The 1st–99th percentiles range in  $M_*$  extends from  $\sim 0.25$ – $6.45 M_{\odot}$ , encompassing both the T Tauri mass regime ( $M_* \lesssim 2 M_{\odot}$ ) and the Herbig Ae/Be mass regime ( $M_* \sim 2$ – $10 M_{\odot}$ ; e.g., Bastien 2015). To evaluate our completeness levels across the stellar mass spectrum, we compared our data to the initial mass function (IMF) expressions presented by Chabrier (2003) for single stars and multiple system populations in the Galactic disk. Earlier studies focused on different star-forming regions (e.g., Moraux et al. 2005) and on the Lagoon Nebula itself (Prisinzano et al. 2005) have shown an overall agreement between the shape of the observed mass

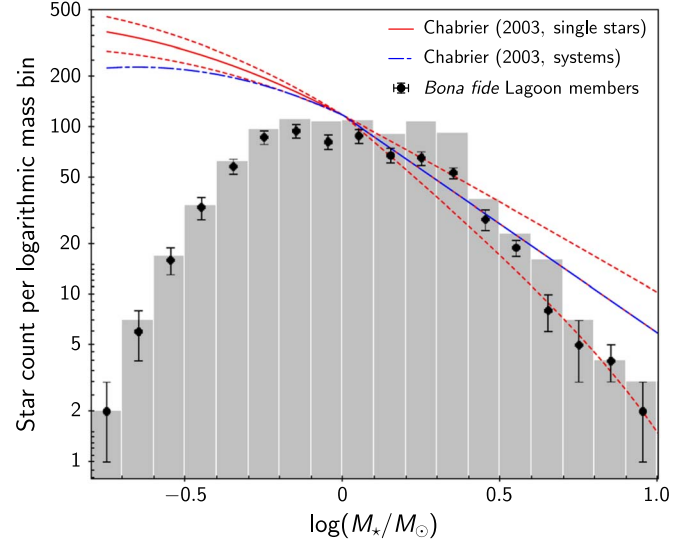


**Figure 3.** Mass distribution inferred for young stars in our Lagoon Nebula sample. The gray histogram refers to the entire population considered in this study, while the black dots and corresponding uncertainties trace the distribution of bona fide members alone. The IMF expressions presented in Chabrier (2003) for single stars (solid red line) and stellar systems (dash-dotted blue line) in the Galactic field are overlaid for comparison purposes, renormalized to the peak of the observed distribution. The dotted red lines trace the range of possible values around the single-star IMF ensuing from the uncertainties on the function parameters tabulated by Chabrier (2003).

distributions in young clusters and the predictions based on the Galactic field IMF. This agreement can be seen in Figure 3 for masses  $M_* > 1 M_{\odot}$ . While the match in absolute value derives from the arbitrary normalization of the IMF to the observed distribution peak, the correspondence between the IMF curve and the declining trend of the star count with increasing mass in this range indicates that at least on a relative scale, the mass spectrum of our sample adequately represents the expected composition of the Lagoon Nebula population. At lower masses, however, our sample appears to be significantly incomplete, with an estimated fraction of missing objects  $\sim 15\%$  at  $M_* \sim 0.85 M_{\odot}$ ,  $\sim 50\%$  at  $\sim 0.55 M_{\odot}$ , and  $\sim 90\%$  at  $\sim 0.3 M_{\odot}$ . These biases have been taken into account when evaluating mass-dependent trends in disk activity for the cluster, as discussed in the following sections. The mass distribution of disk-bearing members peaks at lower values than the center of the distribution measured for disk-free members: the median  $\log M_*$  and the associated interquartile range amount to  $-0.04$  and  $0.41$  in the first case, respectively, and to  $+0.10$  and  $0.50$  in the second case, respectively. This difference between the two mass distributions may reflect distinct disk evolutionary stages for stars of different mass, as examined in Section 7.1.

The median age extracted from the MIST models for the population is  $\log t = 6.3^{+0.4}_{-0.5}$  (or  $\log t = 6.2 \pm 0.4$  for bona fide members alone), slightly older but consistent with the typical age of  $\lesssim 1$  Myr associated with the NGC 6530 cluster (Prisinzano et al. 2019). We note, however, that the average age  $\log t = 5.84 \pm 0.36$  reported by Prisinzano et al. (2019) for NGC 6530 is limited to solar-mass and low-mass cluster members ( $T_{\text{eff}} < 5500$  K); if we applied the same cuts to our member sample, we would obtain a more similar  $\log t = 6.0^{+0.4}_{-0.3}$ . This discrepancy may be due to systematic trends in model-based age predictions for higher-mass (hotter) stars with



respect to lower-mass (cooler) stars on the pre-main sequence (e.g., Hosokawa et al. 2011; Herczeg & Hillenbrand 2015). Disk-bearing stars appear to be slightly younger than the cluster average, with a median  $\log t = 6.1^{+0.5}_{-0.3}$  (or  $\log t = 6.0^{+0.5}_{-0.3}$  among bona fide disk-bearing members alone). This feature, coupled with the larger proportion of disk-free stars in our sample, could also contribute to explaining the slightly older age we measure here for the Lagoon Nebula with respect to the estimate of Prisinzano et al. (2019), which was derived for a population with predominantly disk-bearing/accreting stars. The data point distribution in Figure 2 suggests a considerable age spread among the cluster members, the extent of which (spanning over 2 dex) overlaps with the age ranges previously reported in the literature (Tothill et al. 2008; Prisinzano et al. 2019). Compared to the results of Prisinzano et al. (2019), we find here a larger proportion of older ( $>5$  Myr) sources, but with a strong mass-dependent distribution: among  $M_* \leq 1 M_\odot$  sources, 87% appear to be younger than 5 Myr, while of the sources that are more massive than this threshold, the apparent percentage of  $t < 5$  Myr stars is only 61%. Disregarding the mass dependence (which may be impacted by systematic effects in the model predictions), the subset of  $M_* \leq 1 M_\odot$  that appear older than 5 Myr is characterized by a slightly larger proportion of candidate members (38%) and a smaller proportion of high-confidence disk-free stars (19%) compared to the overall population. This would suggest that a true tail of old (up to  $t \sim 15$  Myr; Prisinzano et al. 2019) cluster members may be mixed with sources that are affected by photometric uncertainties and/or residual disk effects in this region of the HR diagram.

To complete our set of stellar parameters, stellar radii  $R_*$  were also estimated for our targets from the derived  $T_{\text{eff}}$  and  $L_{\text{bol}}$  using the Stefan–Boltzmann law.

## 5. Tracers of Accretion Activity

To trace accretion activity uniformly in our sample, we relied on the VST/OmegaCAM photometry and measured the color excess linked to accretion that can be detected above the photospheric emission level at UV wavelengths ( $u$  band) and in the narrowband  $H\alpha$  filter.

### 5.1. $u - r$ Color Excess

As a first indicator of accretion, following Venuti et al. (2014), we measured the  $u - r$  color excess  $E(u - r)$  in the  $(u - r, r)$  color-magnitude diagram (CMD). As mentioned in Section 3.1, this indicator is available for 486 of the 1012 sources in our sample. We first used the individual  $A_V$  estimates to deredden our photometric data using filter-dependent extinction coefficients calculated from the prescription of Cardelli et al. (1989) at the effective wavelengths of the filters and assuming an anomalous reddening law with  $R_V = 5$  (Prisinzano et al. 2019). The resulting dereddened CMD is illustrated in Figure 4.

In order to measure  $E(u - r)$ , we used the subsample of stars, bona fide members classified as high-confidence disk-free sources, to extract a magnitude-dependent reference color sequence  $(u - r)_{\text{ref}}$  that would trace the photospheric and chromospheric emission level above which accretion activity can be detected. To minimize the impact of color outliers, we removed prior to extracting the reference sequence the few dozen overluminous sources with photometric coordinates that would correspond to presumed ages more than  $2\sigma$  distant from

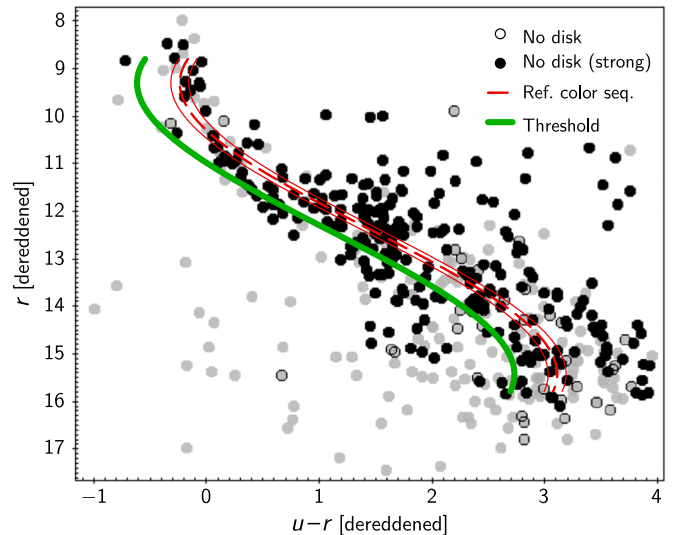


**Figure 4.** Dereddened  $(u - r, r)$  CMD for Lagoon Nebula members in our sample with available  $u$ -band photometry. The objects classified as disk-free are highlighted as black dots (strong classification) and black circles (more uncertain classification). The gray dots without a contour correspond to disk-bearing sources. The dashed and solid red curves trace the median reference color sequence extracted from our high-confidence disk-free population and a photometric range around the sequence ( $\pm 0.08$  mag) that takes into account the uncertainty on the reference fit, respectively. The threshold adopted to select accreting stars is traced in green.

the best-fitting isochrone to the cluster locus. For the retained subsample, we extracted a reference  $r$ -dependent sequence of  $u - r$  colors by implementing a moving median routine in 1 mag wide bins in  $r$  with steps of 0.5 mag. Within each bin, we computed the median  $r$  magnitude ( $\bar{r}$ ) and associated  $u - r$  color and then performed a third-degree polynomial fit to the  $(\bar{r}, \overline{u - r})$  sequence to extract a functional form for the reference  $u - r$  value as a function of  $r$ .

Two different sources of uncertainty are associated with the derived reference color sequence: one component that reflects the discrepancy between the actual median photometric sequence and the fitting curve, which amounts to about  $\pm 0.08$  mag; and another component that reflects the intrinsic scatter of the observed photometric properties for disk-free stars around the reference sequence, estimated to be about  $\pm 0.37$  mag from the typical extent of the interquartile range in  $u - r$  values within each magnitude bin. The quadratic sum of these two sources of uncertainty amounts to  $\sim 0.38$  mag; therefore, we considered as high-probability accretors all targets with  $u - r$  colors that stand at least 0.38 mag below the reference color sequence for disk-free stars.

We defined the excess  $E(u - r) = (u - r)_{\text{obs}} - (u - r)_{\text{ref}}$ , computed for the entire sample of stars regardless of their disk classification. We then used a tiered system to classify our targets according to their accretion status based on the measured  $E(u - r)$ :

1. nonaccreting when  $E(u - r) > -0.08$  (sources to the right of the reference color strip on Figure 4);
2. potential accretors if  $-0.38 < E(u - r) < -0.08$  (sources located between the reference color strip and the lower end of the interquartile range that traces the color dispersion of disk-free sources);
3. accreting when  $E(u - r) < -0.38$  (i.e., located below the first quartile associated with the disk-free color distribution, traced in green on Figure 4).

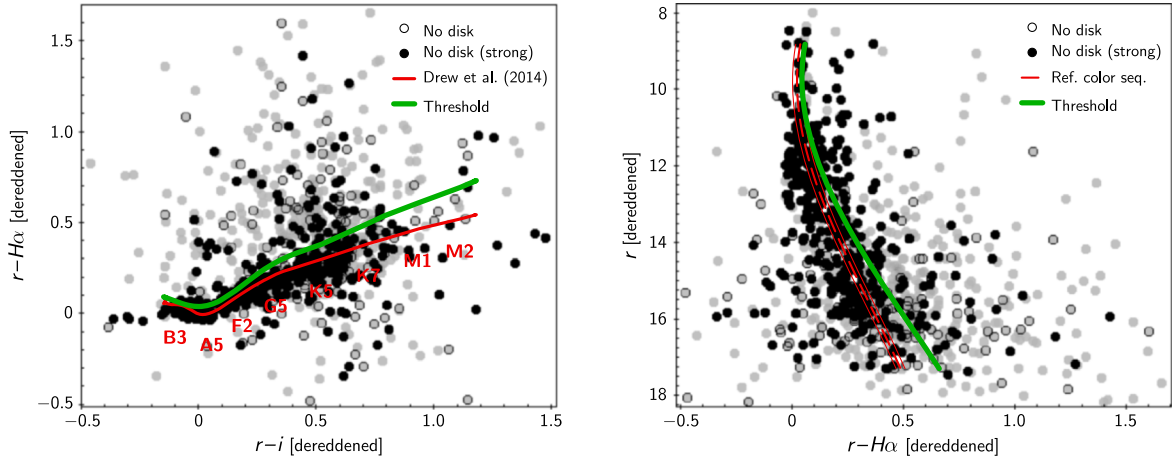


**Figure 5.** Diagnostics of accretion extracted for our target stars from the  $r - H\alpha$  color index on the dereddened ( $r - i$ ,  $r - H\alpha$ ) CCD (left) and ( $r - H\alpha$ ,  $r$ ) CMD (right). The colors and symbols are the same as in Figure 4. In the left panel, the red curve traces the SpT-dependent photospheric color sequence tabulated for main-sequence dwarfs in the VST/OmegaCAM filters by Drew et al. (2014). The spectral types, shifted downwards for clarity, are labeled along the reference sequence to guide the eye. In the right panel, the dashed and solid red curves trace the median reference color sequence extracted from our high-confidence disk-free population and a photometric range around the sequence ( $\pm 0.02$  mag) that takes into account the uncertainty on the reference fit, respectively. In both panels, the threshold curve adopted to select accreting stars is traced with a thicker green line. The stars selected as accretors are located above the green line in the CCD and to the right of the green line in the CMD.

The above procedure resulted in the following statistical classifications:

1. 120 accreting sources (25%), 96 potential accretors (20%), and 270 nonaccreting sources (55%) in the entire sample;
2. 41% accreting sources and 45% nonaccreting sources among all disk-bearing stars (48% accreting sources and 38% nonaccreting sources when limited to stars that were classified as disk-bearing with high confidence);
3. 16% (15%) accreting sources and 63% (64%) nonaccreting sources among all (high-confidence) disk-free stars.

### 5.2. $r - H\alpha$ Color Excess

As a second indicator of accretion activity, we measured the excess  $E(r - H\alpha)$  on the observed  $r - H\alpha$  colors. This approach could be applied uniformly across our sample because 97% of our targets have available  $r$ ,  $i$ ,  $H\alpha$  photometry, as reported in Section 3.1. As a first diagnostic tool, we used the ( $r - i$ ,  $r - H\alpha$ ) color-color diagram (CCD), matching earlier accretion studies conducted on young star clusters (e.g., Kalari et al. 2015).

The procedure we adopted to classify our targets as accreting or nonaccreting based on  $E(r - H\alpha)^{\text{CCD}}$  is illustrated in Figure 5 (left).

Namely, we took as reference the color sequence in the VST/OmegaCAM filters tabulated by Drew et al. (2014), which provides a very good description of the locus traced by the bulk of high-confidence disk-free stars in the diagram. We then defined a color-dependent accretion threshold as the sum of the adopted reference color sequence plus half the typical interquartile range in  $r - H\alpha$  values of the well-characterized disk-free stars as a function of  $r - i$ , which varies between  $\sim 0.02$  mag at  $r - i \simeq -0.15$  and  $\sim 0.18$  mag at  $r - i \simeq 1.17$ . We further defined as potential accretors all stars that have measured  $E(r - H\alpha)^{\text{CCD}}$  between 0.003 mag and the threshold curve, the lower limit being the typical uncertainty on the polynomial fit used to describe the reference color sequence

with respect to the table of Drew et al. (2014). All remaining sources were considered nonaccreting based on  $E(r - H\alpha)^{\text{CCD}}$ .

This procedure resulted in the following statistical classifications:

1. 385 accreting sources (39%), 166 potential accretors (17%), and 428 nonaccreting sources (44%) in the entire sample;
2. 59% (65%) accreting sources and 26% (24%) nonaccreting sources among all (high-confidence) disk-bearing stars;
3. 26% (21%) accreting sources and 54% (59%) nonaccreting sources among all (high-confidence) disk-free stars.

We also conducted a classification of accreting versus nonaccreting sources based on their color distribution in the ( $r - H\alpha$ ,  $r$ ) CMD. The implementation of this procedure is illustrated in Figure 5 (right). Namely, as in Section 5.1, we selected well-characterized disk-free stars and used them to build a reference  $r$ -dependent color sequence above which to calculate the  $r - H\alpha$  color excess  $E(r - H\alpha)^{\text{CMD}}$ . The reference sequence was derived by implementing a moving median technique on  $r$  with the same binning choice as was used in Section 5.1, and a third-order polynomial fit was extracted from the derived  $(\bar{r}, \overline{r - H\alpha})$  sequence. The overall agreement between the fitting polynomial and the actual moving average sequence, as well as the typical interquartile range calculated for the spread in  $r - H\alpha$  of disk-free stars as a function of  $r$ , were taken into account as described in Section 5.1 to derive the classification thresholds above the reference color sequence. A tiered classification scheme mirroring the one implemented in Section 5.1 was then applied to the entire population. A given object was classified as nonaccreting when  $E(r - H\alpha)^{\text{CMD}} < 0.02$ , as a potential accretor when  $E(r - H\alpha)^{\text{CMD}} = [0.02, 0.06]$ , and as accreting when  $E(r - H\alpha)^{\text{CMD}} > 0.06$ .

The results from this classification are as follows:

1. 389 accreting sources (40%), 123 potential accretors (12%), and 467 nonaccreting sources (48%) in the entire sample;

2. 58% (62%) accreting sources and 30% (28%) nonaccreting sources among all (high-confidence) disk-bearing stars;
3. 31% (28%) accreting sources and 56% (59%) nonaccreting sources among all (high-confidence) disk-free stars.

### 5.3. Comparison between Distinct Accretion Diagnostics

The two  $(r - H\alpha)$ -based classification schemes yield very similar proportions of accretors,  $\sim 40\%$  for the entire population, and  $60\%$ – $65\%$  for the disk-bearing sources alone. The somewhat lower percentage of accreting stars selected with the  $E(u - r)$  indicator (25% in the entire sample and up to  $\sim 50\%$  for the disk-bearing stars) can be ascribed to the smaller sample size for which  $u$ -band data are available and to the intrinsically more scattered color distribution of disk-free stars in the  $(u - r, r)$  diagram, which prevents an accurate empirical determination of the reference color sequence for nonaccreting sources.

The classification results obtained for individual objects from different accretion diagnostics show a substantial agreement. Namely, the  $E(u - r)$  classification is consistent with results from the  $E(r - H\alpha)^{\text{CMD}}$  ( $E(r - H\alpha)^{\text{CCD}}$ ) tracer in 67% (82%) of cases for which all indicators are available. The classifications produced by the  $E(r - H\alpha)^{\text{CMD}}$  and the  $E(r - H\alpha)^{\text{CCD}}$  tracers are highly correlated, overall yielding consistent results in 92% of the cases.

### 5.4. Variability of Accretion Tracers and Final Classification

The classification schemes described in Sections 5.1–5.2 are based on the average photometric properties derived for each object during the VST/OmegaCAM observations. However, a more accurate depiction of how individual objects move in the accretion-dominated and photosphere-dominated regions of different color diagrams can be derived by monitoring the variability of the measured color excesses.

As detailed in Venuti et al. (2021), the OmegaCAM survey comprised 17 distinct observing epochs, spread over 3.5 weeks. For each epoch, we measured instantaneous values of the color excesses and then used the classifications extracted from the average photometry as a guide to assess the typical behavior of accreting, nonaccreting, and potentially accreting stars around the accretion thresholds in the various diagrams. Common statistical trends could be identified for the accreting and nonaccreting objects with the various diagnostics. Namely, 90% of the stars classified as nonaccreting were consistently found in the photosphere-dominated regions of the color diagrams in over 70% of observing epochs. Conversely, 75% of objects classified as accreting populated the accretion-dominated regions of the color diagrams in over 80% of epochs. We then merged the single-epoch accretion classifications as follows:

1. for each individual color diagnostics, objects were flagged as accreting, nonaccreting, or potential accretors based on the above statistics (i.e., accreting when they displayed a color excess in  $>80\%$  of epochs, nonaccreting when they appear as such in  $>70\%$  of epochs, and potential accretors otherwise);
2. when all three indicators provided a coherent classification, the leading classification was retained as final accretion status for the corresponding object;

3. if the three indicators provided discrepant classifications (some as accreting sources and others as nonaccreting sources), the prevailing class was retained when it was supported by at least one indicator from each color diagnostics ( $u - r$  and  $r - H\alpha$ ), otherwise, the object was labeled as a potential accretor;
4. the resulting list of potential accretors was subsequently filtered, and a more definite accretion status was assigned when reasonable by considering the prevalence of single-epoch measurements that would classify the object as accreting or nonaccreting, and downgrading flags referred to color excess measurements with large uncertainties.

Our final aggregate classification, reported in Table 1, encompasses 343 accreting sources, 487 nonaccreting sources, and 149 potential accretors. As in Section 3.2, we followed a conservative approach to estimate the true statistical fraction of accreting stars ( $f_{\text{acc}}$ ) in the Lagoon Nebula, accounting for classification uncertainties and missing data. This approach resulted in  $f_{\text{acc}} = 0.38 \pm 0.10$  for the entire population and  $f_{\text{acc}} = 0.41 \pm 0.11$  when considering bona fide members alone. Accreting sources represent 54% of the targets that are classified as high-confidence disk-bearing stars and 17% of the targets that are classified as high-confidence disk-free stars. Nearly 86% of the high-confidence disk-bearing sources classified as accreting were detected in accretion at all epochs during our monitoring campaign, whereas about one-third of the disk-free stars in the accreting group were detected in accretion only at certain epochs, indicating that these objects may currently be evolving past the disk accretion stage. Nonaccreting sources represent 26% of our sample of high-confidence disk-bearing stars and 68% of our sample of high-confidence disk-free stars. A comparison between the final disk status and accretion status classifications for our sample of YSOs with respect to  $\alpha_{\text{IRAC}}$  and  $E(r - H\alpha)^{\text{CCD}}$  is illustrated in Figure 6.

Disk-free stars flagged as accreting are concentrated predominantly (in  $\sim 83\%$  of cases) at later spectral types (G, K, M), exceeding the statistical proportion of G-to-M types that is found for the entire population of disk-free stars. While an intense chromospheric activity may in some cases affect the selection of individual objects as accretors based on the  $H\alpha$  diagnostics, independent spectroscopic information available from the literature for this subset tends to support the reliability of our statistical classification. In particular, Prisinzano et al. (2019) used the VLT/FLAMES spectra obtained for NGC 6530 members within the GES program to measure the full width at zero intensity (FWZI) of the  $H\alpha$  line, which provides an accretion indicator where the impact of nebular contamination to the stellar spectra is minimized compared to other  $H\alpha$  diagnostics that rely on the line core intensity (e.g., Bonito et al. 2020). Of the 29 targets that represent the intersection between our high-confidence disk-free sample, our sample of accreting stars, and the sample of NGC 6530 members with FWZI measurement from Prisinzano et al. (2019), 23 (79%) are located above the FWZI = 4 Å threshold adopted in that paper to select candidate accretors, and 19 (66%) have FWZI  $> 5$  Å, quoted by the authors as the empirical value above which known disk-bearing/accreting stars in their sample were distributed. Additional  $H\alpha$  spectroscopic measurements from VLT/FLAMES spectra simultaneous with K2 Campaign 9 (program 097.C-0387(A), PI = S. Alencar) are available for a small subset (40 objects) of our



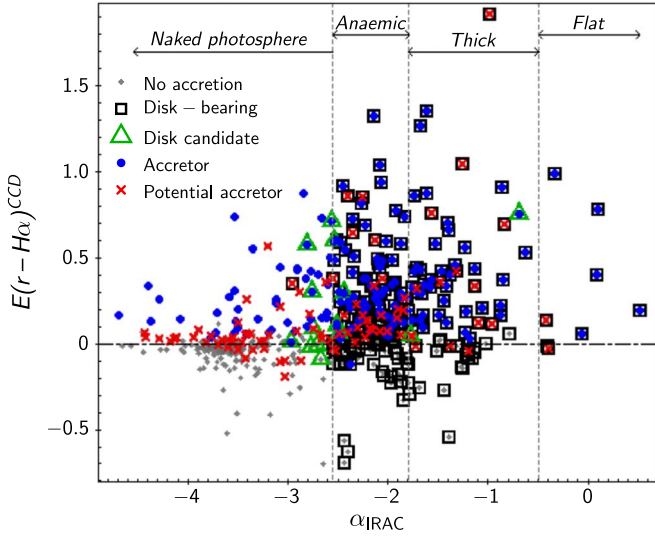


**Figure 6.** Distribution of Lagoon Nebula YSOs according to their accretion properties (as traced via  $E(r-H\alpha)^{CCD}$ , Section 5.2) vs. disk properties (as traced via  $\alpha_{IRAC}$ , Section 3.2). The colors and symbols denote the final accretion/disk classifications derived for each object from our analysis: small gray dots are stars without evidence of accretion from all available indicators, blue dots are accreting sources, red crosses are potential accretors, black squares surround disk-bearing sources, and green triangles surround disk candidate sources. The disk class labels at the top of the figure follow the  $\alpha_{IRAC}$  scheme by Teixeira et al. (2012).

target list, which includes only two stars classified as disk-free but accreting in our sample. Our photometric classification of sources as accreting, potential accretors, or nonaccreting agrees with the derived spectroscopic information for all except five objects in this subset (88%). Of the two disk-free sources with photometric indicators of accretion included in the subset, at least one (EPIC 248368907) shows clear spectroscopic evidence of accretion as well, with a measured  $H\alpha$  width at 10% intensity  $\sim 600 \text{ km s}^{-1}$ .

The nature of these objects with seemingly contrasting disk/accretion classifications can at least partly be understood in terms of more evolved circumstellar disks. As reviewed by Espaillat et al. (2014), young clusters and star-forming regions as young as a few Myr are expected to comprise  $\sim 3.5\%$ – $7\%$  transition disk sources with large inner cavities that are no longer traceable in the near-IR. If this were applied to our sample, it would translate into  $\sim 35$ – $70$  transition disk candidates for the entire population and  $\sim 30$ – $60$  for our subset of objects with IR data. A vast fraction of transition disk sources in young open clusters can exhibit accretion levels comparable to those of primordial disk sources (e.g., Sousa et al. 2019). For about two-thirds of the accreting disk-free stars in our sample, only  $J$ ,  $H$ ,  $K$  photometry was available to categorize their evolutionary status, which implies that a putative transition disk around them could not have been detected. The remaining one-third had available Spitzer/IRAC photometry that identified them as naked photospheres following the scheme of Teixeira et al. (2012). While the corresponding  $\alpha_{IRAC}$  values are somewhat lower than the typical anaemic disk indices extracted for transition disks in IRAC bands, similar  $\alpha_{IRAC}$  ranges have been tabulated by Sousa et al. (2019) for about 20% of their transition disk candidates.

## 6. Disk Accretion in the Lagoon Nebula

### 6.1. Accretion Rates and Connection with $M_*$

To convert the color excesses into estimates of the accretion luminosity  $L_{acc}$ , we followed the approaches of Venuti et al. (2014) and Kalari et al. (2015). Namely, we defined the flux excess due to accretion,  $F_{exc}$ , as

$$F_{exc} = F_{obs} - F_{phot}, \quad (1)$$

where  $F_{obs}$  is the stellar flux calculated from the dereddened magnitude, and  $F_{phot}$  is the contribution from photospheric and chromospheric activity. Assuming that the accretion luminosity only affects the  $u$  and  $H\alpha$  observations (not the  $r$  band), we can define the photospheric  $u$  and  $H\alpha$  magnitudes as  $u_{phot} = u_{obs} - E(u-r)$  and  $H\alpha_{phot} = H\alpha_{obs} + E(r-H\alpha)$ . From Equation (1), we can then derive  $F_{exc}^u$  and  $F_{exc}^{H\alpha}$  as

$$F_{exc}^u = F_0^u \cdot 10^{-0.4 \cdot u_{obs}} (1 - 10^{+0.4 \cdot E(u-r)}) \quad (2)$$

and

$$F_{exc}^{H\alpha} = F_0^{H\alpha} \cdot 10^{-0.4 \cdot H\alpha_{obs}} (1 - 10^{-0.4 \cdot E(r-H\alpha)}), \quad (3)$$

where  $F_0^u$  ( $1.2445 \times 10^{-6} \text{ erg cm}^2 \text{ s}^{-1}$ ) and  $F_0^{H\alpha}$  ( $1.84 \times 10^{-7} \text{ erg cm}^2 \text{ s}^{-1}$ , corresponding to  $H\alpha$ -mag  $\simeq 0.03$ ; Drew et al. 2014) are the  $u$ -band and  $H\alpha$ -band integrated zeropoint fluxes, respectively. The excess luminosity  $L_{exc}$  is then calculated as  $L_{exc} = F_{exc} \cdot 4\pi d^2$ , where  $d$  is the adopted distance to the cluster. To convert the filter-specific  $L_{exc}$  into total accretion luminosity  $L_{acc}$ , we followed the prescription by Venuti et al. (2014) for the  $u$ -band excess measurement and the calibration relations between  $L_{exc}^{H\alpha}$  and  $L_{acc}$  derived by Alcalá et al. (2017) for the T Tauri regime and by Fairlamb et al. (2017) for the Herbig (A/B) regime, after verifying that all A/B stars in our sample match the ranges in mass and absolute magnitude presented in Vioque et al. (2022) and Vioque et al. (2020), respectively, for confirmed and candidate Herbig Ae/Be stars. Finally, the mass accretion rate  $\dot{M}_{acc}$  is estimated as

$$\dot{M}_{acc} = \left(1 - \frac{R_*}{R_{in}}\right)^{-1} \frac{L_{acc} R_*}{GM_*}, \quad (4)$$

where  $G$  is the gravitational constant, and  $R_{in}$  is the infall radius for the accretion column, assumed to correspond to the truncation radius at  $\sim 5 R_*$  in the T Tauri regime and  $\sim 2.5 R_*$  in the Herbig regime (Mendigutía et al. 2011).

The  $\dot{M}_{acc}$  values inferred from the three color diagnostics are largely consistent with each other, with the following median offsets:

1.  $\log \dot{M}_{acc}^{(u-r)} - \log \dot{M}_{acc}^{(r-H\alpha)_{CCD}} \simeq 0.1^{+0.5}_{-0.4}$
2.  $\log \dot{M}_{acc}^{(u-r)} - \log \dot{M}_{acc}^{(r-H\alpha)_{CMD}} \simeq -0.1^{+0.4}_{-0.3}$
3.  $\log \dot{M}_{acc}^{(r-H\alpha)_{CCD}} - \log \dot{M}_{acc}^{(r-H\alpha)_{CMD}} \simeq 0.04^{+0.06}_{-0.05}$ .

A final typical value of  $\dot{M}_{acc}$  was assigned to each source by taking the median of the central values derived from each color diagnostics, while variability bars were derived by calculating the range between median and minimum/maximum values of the instantaneous  $\dot{M}_{acc}$  measured along the entire monitored period with VST/OmegaCAM. These parameters are reported for all available targets in Table 1. Objects that fell below the accretion detection thresholds in color (see Section 5), at least at some epochs, were marked as upper limits without a defined

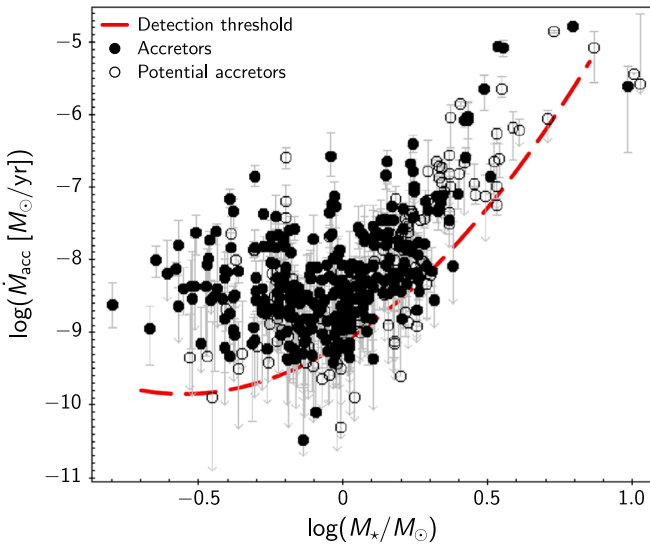


**Figure 7.** Accretion rate distribution as a function of stellar mass for Lagoon Nebula stars classified as accreting (black dots) or potential accretors (empty circles). Variability bars mark the full range of  $\dot{M}_{\text{acc}}$  values measured during the VST/OmegaCAM monitoring. Upper limits, marked as downward arrows, are assigned to objects that were located in the nonaccreting regions of the various color excess diagrams at least in some epochs. The dashed red line traces a reference detection threshold, derived as a polynomial fit to the nominal  $\dot{M}_{\text{acc}}$  values extracted for stars classified as nonaccreting following the criteria discussed in Section 5.4.

lower variability bar. The resulting  $\dot{M}_{\text{acc}}$  distribution as a function of  $M_*$  is illustrated in Figure 7.

To extract any mass-dependent trends in  $\dot{M}_{\text{acc}}$ , we measured the median logarithmic  $\dot{M}_{\text{acc}}$  in 0.2 dex wide logarithmic mass bins using a 0.1 dex wide moving window. This analysis was only conducted in the mass range  $-0.7 < \log M_* < 0.8$  to ensure the presence of at least four accreting sources in each bin, and it revealed distinct  $M_* - \dot{M}_{\text{acc}}$  regimes: a substantially flat trend for  $\log M_* < 0$ ; a monotonically increasing trend in  $\log \dot{M}_{\text{acc}}$  for  $\log M_*$  between 0 and 0.6; and a potential flattening in the  $M_* - \dot{M}_{\text{acc}}$  trend that begins to emerge at  $\log M_* \geq 0.6$ . We then followed the approach discussed in Vioque et al. (2022) to refine our search for the transition values of  $\log M_*$ . Namely, we let the test value of logarithmic transition mass vary across the entire range covered by two consecutive regimes, as identified earlier (i.e., from  $-0.7$  to  $0.6$  in the first case, and from  $0$  to  $0.8$  in the second case). We used each test value to split the corresponding sample of objects into two mass groups, and we applied a linear regression routine to calculate the best-fitting slope for both groups separately. We then estimated the significance of the slope difference between the two groups, weighted by the uncertainty on the derived slopes, and we built a distribution of this significance parameter as a function of the assumed transition mass. Finally, we defined our best estimate of the logarithmic transition mass as the value that maximizes the significance of the difference in slope between the two neighboring mass groups. This procedure allowed us to extract a robust estimate of the first transition point at  $\log M_* \approx 0.01$ , with a best-fitting slope of  $\log \dot{M}_{\text{acc}} = (4.5 \pm 0.3) \cdot \log M_* + k$ , to describe the  $M_* - \dot{M}_{\text{acc}}$  relation in the intermediate-mass regime, and a typical value of  $\log \dot{M}_{\text{acc}} \approx -8.6$  for the flat distribution of accretion rates at masses  $\log M_* \leq 0.01$ .

Given the small number of objects at the high-mass end of our distribution, we could only obtain a rough lower limit of

$\log M_* \approx 0.61$  for the second potential transition point. We note that this lower limit (at  $M_* \sim 4.07 M_\odot$ ) is consistent with the better-defined mass value at which a break in the  $M_* - \dot{M}_{\text{acc}}$  relation for Herbig AeBe stars has been reported by Wichittanakom et al. (2020;  $M_* = 3.98^{+1.37}_{-0.94} M_\odot$ ) and Vioque et al. (2022;  $M_* = 3.87^{+0.38}_{-0.96} M_\odot$ ). A positive correlation trend between  $\log \dot{M}_{\text{acc}}$  and  $\log M_*$  was reported by the same authors for the higher-mass component of the Herbig AeBe population, albeit shallower than the one found among less massive Herbig AeBe stars. No such trend can be decisively extracted from our data due to the dearth of objects at masses higher than  $\log M_* \sim 0.5$  in our sample. On the other hand, the slope extracted in the logarithmic mass range  $\approx 0 - 0.6$  is at least qualitatively consistent with the trend traced for lower-mass Herbig AeBe stars in Vioque et al. (2022), and it overlaps with the slope intervals for the lower-mass group estimated by Wichittanakom et al. (2020). The overall flat trend observed at the lower-mass end of our distribution in Figure 7 ( $-0.5 \leq \log M_* \leq 0$ ) qualitatively matches analogous trends observed in the same mass range in different star-forming regions (e.g., Venuti et al. 2014), although the median  $\log \dot{M}_{\text{acc}}$  value extracted here appears to be somewhat lower than those reported for other young stellar populations. This feature, coupled with the lower frequency of some irregular disk-driven variables (bursting, stochastic, aperiodic dippers) that are identified in the Lagoon K2 sample (Venuti et al. 2021) compared to other young clusters surveyed from space (Cody et al. 2014; Cody & Hillenbrand 2018; Cody et al. 2022), may indicate more moderate accretion dynamics in the Lagoon Nebula cluster.

When we analyze the typical accretion properties detected for specific variable groups with respect to those measured in the entire population as a function of mass, we do observe some correlation with the light-curve morphology class. The one burster star with a mass estimate in our sample is located in the top quartile of the  $\dot{M}_{\text{acc}}$  distribution for the corresponding mass bin. Stochastic variables have typical accretion rates higher than the median measured across the entire population in 80% of the mass bins where they are represented, while the same is true for flat-line variables in  $\sim 60\%$  of the mass bins where they appear; for aperiodic dippers in  $\sim 55\%$  of mass bins; for periodic and multiperiodic variables and quasi-periodic dippers in  $\sim 40\%$ – $45\%$  of mass bins; and for quasi-periodic symmetric variables in 25% of mass bins.

## 6.2. Wavelength-dependent Trends in Photometric Light Curves for Accreting Stars

In the magnetospheric accretion framework, hot spots at the stellar surface are predicted to be structured in density, with a more compact ( $\lesssim 1\%$  area) high-density region emitting predominantly at shorter wavelengths, and a more extended ( $\gtrsim 10\%$ – $20\%$ ) low-density region emitting predominantly at longer wavelengths (e.g., Romanova & Owocki 2015). This radial gradient in the hot-spot density profile is expected to translate into a wavelength-dependent apparent size for the hot spot itself and into a slightly asynchronous nature in the spot-induced variability patterns at different filters. Recently, a first direct observational confirmation of the latter prediction has been obtained for the young accreting star GM Aur by Espaillat et al. (2021), who monitored the star from the  $u$  to the  $i$  band and detected a significant delay in the appearance of luminosity

peaks at optical wavelengths with respect to their timing in the near-UV.

Unfortunately, the sparser cadence of our ground-based monitoring data does not allow us to perform a precise peak-timing analysis. However, we did conduct a statistical exploration of wavelength-dependent trends in the light-curve morphology of our accreting targets by taking as reference the K2 time series. More specifically, after rejecting  $>5\sigma$  discrepant points and removing any underlying systematic trends, all K2 light-curve points between the 1st–99th percentiles in flux were selected, and a brightness phase was defined as

$$\phi_i^{\text{flux}} = \frac{f_i - f_{\min}}{f_{\max} - f_{\min}}, \quad (5)$$

where  $f_i$  is the normalized flux at epoch  $i$ , and  $f_{\min}$  and  $f_{\max}$  correspond to the percentile levels defined earlier. We then matched each VST/OmegaCAM observing epoch with the closest K2 observation and defined a corresponding value of the expected  $\phi^{\text{flux}}$  as the median  $\phi_i^{\text{flux}}$  within a range of five K2 epochs around the best-matching date.

To assess the overall agreement between the photometric variations traced at  $u$ ,  $g$ ,  $r$ ,  $i$  wavelengths and the K2 light curves, we applied a Spearman rank correlation test as implemented in the Python module `scipy.stats` to the array of  $(\text{mag}, \phi^{\text{flux}})$  values obtained for each band. In case of a perfect correspondence between the K2 light-curve pattern and the magnitude trends in a given VST/OmegaCAM filter, we would expect to observe a definite anticorrelation trend between the two quantities in the array (i.e., lower magnitude values corresponding to higher values of  $\phi^{\text{flux}}$ ), leading to a negative rank correlation coefficient  $\rho$  that approaches unity. Conversely, OmegaCAM and K2 light curves in opposition of phase would lead to positive  $\rho$  values because increases in magnitude in the ground-based time series would be matched by high  $\phi^{\text{flux}}$  values (extracted from the K2 time series).

To probe whether the agreement between K2 and each of the individual  $u$ ,  $g$ ,  $r$ ,  $i$  light curves would be improved by assuming a time shift between the two time series, we repeated the analysis described above by imposing a lag  $\Delta t$  when matching the VST and K2 epochs. In our exploration, we let  $\Delta t$  vary between  $-2$  days and  $+2$  days, and at each step we assigned a best-matching K2 epoch ( $t_{\text{K2}}$ ) to each VST epoch ( $t_{\text{VST}}$ ) as the one that minimized  $|t_{\text{VST}} - (t_{\text{K2}} - \Delta t)|$ . For each object and filter, we then examined the resulting values of  $\rho$  as a function of  $\Delta t$ . An illustration of this procedure for the accreting young star SCB680 is shown in Figure 8.

For regular variables, an underlying periodic pattern in the  $(\Delta t, \rho)$  trend is expected, corresponding to the rotation rate  $P_{\text{rot}}$  of the star. Small deviations from this periodicity may reveal distinctive trends in the appearance of variability features as a function of wavelength. To extract any such trends from our light curves, we conducted a sinusoidal fit on the  $(\Delta t, \rho)$  distribution filter by filter using the `scipy` function `optimize.curve_fit`, and defining our model function as

$$\rho = a \cdot \sin(b \cdot \Delta t - c) + d. \quad (6)$$

We restricted this exploratory analysis to accreting YSOs in the Lagoon Nebula with light curves classified as periodic or quasi-periodic, and assigned initial values for the fit parameters as  $a_0 = 0.5 \cdot (\rho_{\max} - \rho_{\min})$ ,  $b_0 = 2\pi/P_{\text{rot}}$ ,  $c_0 = 0$ , and  $d_0 = 0.5 \cdot (\rho_{\max} + \rho_{\min})$ . To interpret the results, we then focused

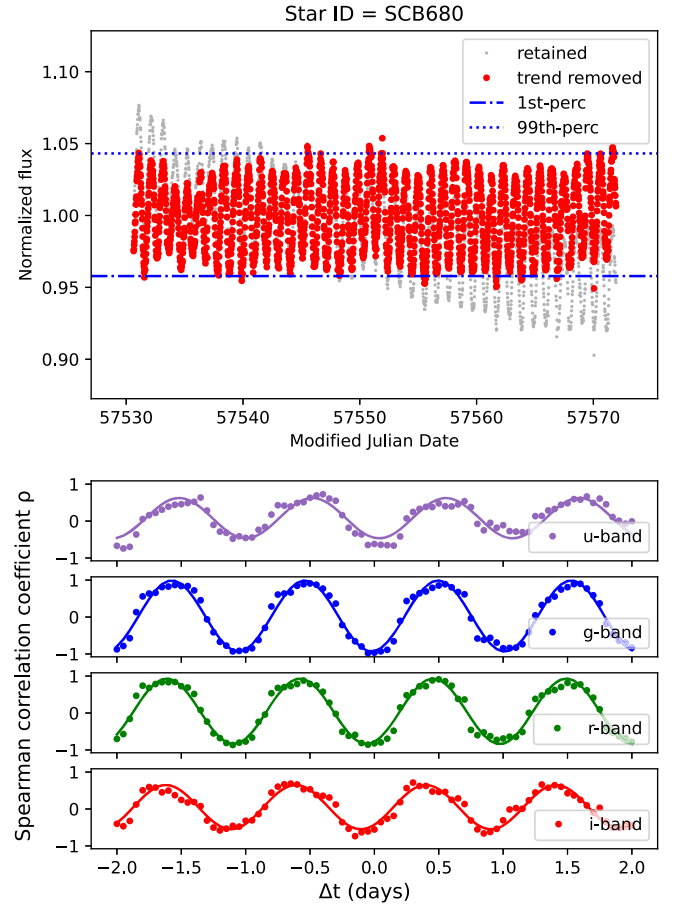


**Figure 8.** Example of a periodic K2 light curve for a young accreting star in the Lagoon Nebula (top) and results of the correlation analysis between the K2 time series and each of the  $u$ ,  $g$ ,  $r$ ,  $i$  light curves as a function of the hypothetical time lag between the respective variation patterns (bottom), as described in the text. The overlaid curves in the bottom panel represent sinusoidal fits to the measured  $(\Delta t, \rho)$  trends.

on the best-fit parameters  $b$  and  $c$ , which are related to the periodicity  $P$  and time shift  $\tau$  of the sinusoid as  $P = 2\pi/b$  and  $\tau = -c/b$ . In this formulation, negative values of  $\tau$  indicate a delay in the sinusoid.

A successful sinusoidal fit with an optimal solution was achieved for 27 of the 40 accreting stars with well-behaved regular light curves in our sample. Some interesting trends emerged from these results. In 21 of the 27 cases, a definite trend in the measured  $P$  as a function of wavelength could be identified: in 57% of the cases, the measured  $P$  overall increases from the  $u$  to the  $i$  band (typical change  $\sim 18\%$  of the  $u$ -band period), while in the remaining 43% of cases,  $P$  is found to decrease from  $u$  to  $i$  (with a smaller typical change of  $\sim 6\%$  in  $P$ ). For comparison, the maximum uncertainties on  $P$  as measured from the K2 light curves amount to 4%–8% for the least periodic cases in our subset, and for a case such as the one illustrated in Figure 8, the estimated uncertainty on  $P$  is  $<1\%$ . No obvious connection was observed between the specific trend in  $P$  and stellar parameters such as  $M_*$  and SpT, but stars in this subset that were consistently observed as accreting at all VST/OmegaCAM epochs were found to preferentially exhibit an increase in  $P$  from  $u$  to  $i$  (77% of the cases), whereas 71% of stars in the subset that only appeared as accreting at some epochs were found to exhibit a  $P$  that decreases from  $u$  to  $i$ .



While a detailed modeling of these behaviors is beyond the scope of this work, we note that drifts in the measured period as a function of wavelength may reflect slightly different intrinsic timescales for the features that dominate the emission detected in separate filters. As discussed in Espaillat et al. (2021, see in particular their Figure 4), the differential rotation between the stellar magnetosphere and the inner disk may induce a dragging effect on the accretion funnels, triggering changes in both the shape and location of the hot spots. As a consequence, the hot-spot modulation pattern would be slightly out of sync with respect to the rotation rate of the star. Because the structure of the densest hot-spot regions is particularly affected by these dynamics, nonstationary effects in variability would be observed more predominantly in bluer filters, leading to potential differences in the characteristic timescales extracted from different wavelength regimes.

Regarding  $\tau$ , a time shift between the  $u$  and  $i$  band was detected to a significance of at least  $\sim 2\sigma$  for 18/27 stars in our subset. For the vast majority (16, i.e.,  $\sim 90\%$ ) of them, a positive  $\Delta\tau$  between  $u$  and  $i$  was measured, indicating that the  $u$ -band variability pattern is ahead with respect to the  $i$ -band variability pattern. The median time difference between  $u$  and  $i$  across the 16 targets amounts to  $\sim 7\%$  of the corresponding rotation period measured for each star from the K2 light curve. However, these statistics are highly correlated with the specific  $P$  versus wavelength trends discussed above: for the stars with  $P$  decreasing from the  $u$  to the  $i$  band, we measured a typical  $\Delta\tau/P_{\text{rot}} = 0.34 \pm 0.06$ , while for the stars with  $P$  increasing from  $u$  to  $i$ , we found  $\Delta\tau/P_{\text{rot}} = 0.06 \pm 0.04$ .

### 6.3. Variability and Time Dependence of Accretion

For 275 sources of our sample, we have recorded detectable accretion levels at all epochs during the OmegaCAM monitoring. The median  $\dot{M}_{\text{acc}}$  variability amplitude (and relative dispersion) measured for this subset of objects amounts to  $0.5^{+0.3}_{-0.2}$  dex, consistent with results reported earlier for various young stellar populations (e.g., Costigan et al. 2014; Venuti et al. 2014). Slightly different variability amplitudes above ( $\Delta\dot{M}_+$ ) and below ( $\Delta\dot{M}_-$ ) the median  $\dot{M}_{\text{acc}}$  were statistically measured in the sample ( $0.21^{+0.11}_{-0.09}$  dex and  $0.28^{+0.28}_{-0.14}$  dex, respectively), but the two values overlap well within the scatter. No significant dependence of the  $\dot{M}_{\text{acc}}$  variability amplitude on  $M_*$  was observed.

Some marginal trends in  $\dot{M}_{\text{acc}}$  variability can be extracted from the comparison with the morphological classification of the light curve for sources with K2 data. Flat-line variables tend to exhibit the largest amplitudes of  $\dot{M}_{\text{acc}}$  variability over rotational timescales ( $\Delta\dot{M} \sim 0.6$  dex), followed by quasi-periodic symmetric and aperiodic dipper variables ( $\Delta\dot{M} \sim 0.5$  dex), periodic and stochastic variables ( $\Delta\dot{M} \sim 0.4$  dex), quasi-periodic dippers ( $\Delta\dot{M} \sim 0.3$  dex), and our only burster variable with  $\dot{M}_{\text{acc}}$  estimate ( $\Delta\dot{M} \sim 0.2$  dex). Larger  $\Delta\dot{M}$  would indicate a stronger dependence of the observed accretion rate on the instantaneous viewing geometry, or more intermittent accretion levels on the inner disk dynamical timescales. Smaller  $\Delta\dot{M}$ , on the other hand, would imply a nearly constant visibility of surface accretion features or a homogeneous distribution of accretion streams, coupled with accretion dynamics able to sustain similar  $\dot{M}_{\text{acc}}$  levels over several rotational cycles.

To assess any longer-term  $\dot{M}_{\text{acc}}$  variability trends, we compared our results with those obtained by Kalari et al. (2015), who measured accretion rates for low-mass stars in the

Lagoon Nebula using observations taken four years earlier with the same instrument (OmegaCAM). We cross-correlated our catalog with theirs and could retrieve 100 sources common to both samples (within a  $1''$  matching radius) and with detected  $\dot{M}_{\text{acc}}$  in both studies. For this subset of objects, the typical difference between the single-epoch  $\dot{M}_{\text{acc}}$  measurement reported by Kalari et al. (2015) and the median value of  $\dot{M}_{\text{acc}}$  reported here amounts to  $\Delta(\log \dot{M}_{\text{acc}}) = 0.55 \pm 0.35$  in the logarithmic mass range from  $-0.4$  to  $0.4$ . This value is well consistent with the combined  $\log \dot{M}_{\text{acc}}$  uncertainties and variability bar for a typical star common to this and the study of Kalari et al. (2015;  $\sim 0.75$  dex).

No specific association between the amount of accretion variability measured on timescales of several years and the photometric light-curve behavior (modulated versus erratic versus dipping) emerged for stars with long-term variability information and K2 light curves (34 objects). However, we note that only three YSOs in this subset ( $\sim 9\%$ ) exhibit  $\dot{M}_{\text{acc}}$  variations over several years that stand more than three times above the typical population value in units of the associated dispersion, and all three of them (EPIC IDs 224321494, 224324884, and 224321735) belong to the erratic variable group.

Finally, we examined the connection between the typical  $\dot{M}_{\text{acc}}$  values measured for sources across the Lagoon Nebula and their estimated ages, as derived in Section 4.5. While individual ages extracted for pre-main-sequence YSOs on the HR diagram are notoriously uncertain (e.g., Soderblom et al. 2014), the fundamental stellar and accretion properties that we determined within our sample support an evolutionary scenario that is reflected in the population spread across the isochrone grid in Figure 2. Namely, when our accreting sources are divided into spectral classes, a statistically significant anticorrelation trend emerges between individual  $\dot{M}_{\text{acc}}$  and isochronal ages in each group from A to M stars, with  $p$ -values  $< 0.001$  resulting from a two-sided Spearman rank-order correlation test and Kendall rank correlation coefficient, as verified by performing a permutation test. These anticorrelation trends are illustrated in Figure 9, where the linear fits overlaid on each SpT group were derived using the Theil-Sen estimator to obtain an unbiased approximation of the true slope. This association would suggest the presence of an intrinsic age spread among Lagoon Nebula YSOs, with accretion decreasing as stars become older (e.g., Beccari et al. 2010). The lower agreement between the data point distribution and the simple linear regression result for B-type stars reflects the smaller sample size and comparatively larger scatter, which translates into a more uncertain anticorrelation trend with a  $p$ -value  $\sim 0.15$ .

## 7. Discussion

### 7.1. Mass Dependence of Disk and Accretion Properties

To investigate any connection between disk activity and stellar mass in the Lagoon Nebula, we used the statistical approach presented in Section 3.2 to extract SpT-dependent estimates of  $f_{\text{disk}}$  and  $f_{\text{acc}}$  for our sample. Only stars with both disk and accretion indicators available (814) were used to define the observed sample size and measured fractions. To account for the mass-dependent completeness levels shown in Figure 3, we used the mass distribution of young stars with measured parameters in each spectral class to estimate the

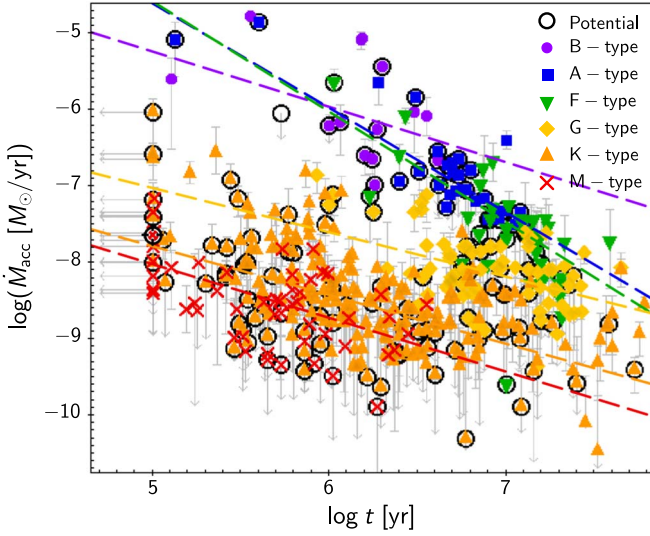


**Figure 9.** Correlation trend between the estimated ages and  $\dot{M}_{\text{acc}}$  values for accreting Lagoon Nebula members as a function of spectral class (colors and symbols are as labeled in the legend). Stars classified as potential accretors are encircled in black. The dashed lines mark the linear trend corresponding to the best-fit slope and intercept derived using the Theil-Sen estimator, with colors matching the corresponding spectral class.

number of missing objects. We then introduced this estimate as a correction to the true population size, which was used to simulate the intrinsic  $f_{\text{disk}}$  and  $f_{\text{acc}}$  that are statistically compatible with the observed fractions of disk-bearing and accreting objects as a function of SpT. Moreover, to explore the timescales of disk clearing with respect to the duration of the accretion phase, we conducted this analysis separately for the subset of stars in our sample for which mid-IR data from Spitzer/IRAC could be used to determine the disk status (496) and for those for which only near-IR data (2MASS) were available (318).

The results of this statistical exploration are shown in Figure 10. Although individual points overlap due to the combined uncertainties related to sample incompleteness and indefinite classifications (i.e., disk candidates, potential accretors), some mass-dependent trends emerge from this picture. Along the horizontal axis on the left panel, which probes the prevalence of disks detectable at mid-IR wavelengths, lower-mass stars (G, K, M spectral types) tend to exhibit higher values of  $f_{\text{disk}}$  than more massive stars. The typical difference in the central  $f_{\text{disk}}$  value estimated for G, K, M stars with respect to B and F stars amounts to  $\sim 17\%$ , or over half of the estimate extracted for B and F stars. In other words, disks around G, K, M stars appear to be about 1.5 times more frequent than around B and F stars. The statistical estimates of  $f_{\text{acc}} - f_{\text{disk}}$  ratios are distributed around the equality line in this diagram, indicating a substantial agreement in the evolutionary dynamics probed by  $\alpha_{\text{IRAC}}$  and accretion diagnostics.

A different picture appears in the right panel of Figure 10, which illustrates the statistical information extracted from stars for which only  $J$ ,  $H$ ,  $K$  photometry could be used to assess the disk status. Compared to the mid-IR sample depicted on the left, a clear drop in the estimated  $f_{\text{disk}}$  ranges can be observed for all mass groups, which suggests that the process of inside-out disk clearing has already begun at the Lagoon Nebula age. However, the statistical  $f_{\text{acc}}$  ranges estimated from the near-IR subset are consistent with those determined from the mid-IR subset for most SpT groups, resulting in an overall shift of the

$f_{\text{acc}} - f_{\text{disk}}$  ratios, which largely lie above the equality line on this diagram. This discrepancy between the measured  $f_{\text{acc}}$  and  $f_{\text{disk}}$  may reflect distinct evolutionary timescales for the gas and dust contents of the inner regions of protoplanetary disks. Indeed, recent numerical studies (e.g., Appellgren et al. 2020) have shown that following an initial phase of slow dust drifting at  $t < 1$  Myr, the dust within the disk can be drained quickly even as the gas accretion rate remains approximately constant. Several factors can contribute to setting the duration of the dust disk clearing phase, including the disk mass (with more massive disks being more common around higher-mass stars; e.g., Rillinger et al. 2023), and the photoevaporation induced by the stellar X-ray luminosity (e.g., Kimura et al. 2016), which is typically more intense for higher-mass YSOs compared to lower-mass objects (e.g., Jardine et al. 2006). Although no conclusive relative ordering of  $f_{\text{acc}} - f_{\text{disk}}$  ratios as a function of SpT can be extracted from the right panel of Figure 10, a faster disk evolution for higher-mass stars than for lower-mass stars in the Lagoon Nebula is suggested by the difference in the steepness of the respective age-dependent trends in Figure 9.

The measurement of higher  $f_{\text{disk}}$  for lower-mass stars is overall consistent with the results of earlier statistical surveys of disk fractions that employed similar photometric criteria for the disk classification. In particular, Ribas et al. (2015) analyzed a sample of  $\sim 1400$  young stars from 22 nearby star-forming regions and found that disk evolution occurs more rapidly around higher-mass stars ( $M_{\star} > 2M_{\odot}$ ) than around lower-mass stars. This effect could already be discerned at very young ages ( $\sim 1\text{--}3$  Myr): indeed, low-mass YSO populations falling into that age bin in Ribas et al.’s (2015) sample were found to exhibit a fraction of protoplanetary disks that amounted to over 1.6 times the  $f_{\text{disk}}$  measured around higher-mass stars in the same regions. We note that while this trend provides a qualitative match to our findings, the absolute values of  $f_{\text{disk}}$  extracted by Ribas et al. (2015) on nearby stellar associations and star-forming regions are significantly higher than the disk fractions derived here. Our estimate in Section 3.2, however, is consistent with the prevalence of IR excess sources among the total population of probable Lagoon Nebula members reported by Povich et al. (2013) from the MYStIX project (Feigelson et al. 2013). This would suggest that the target regions of Ribas et al. (2015) may be subject to very different environmental feedback on disk evolution than the Lagoon Nebula as a whole, although evidence for a possible gradient in conditions across the latter complex has also been reported (e.g., Richert et al. 2018).

In a complementary approach, van der Marel & Mulders (2021) investigated the evolution of protoplanetary disks as a function of the host star mass by studying the occurrence of disk substructures from ALMA data. In their survey, also focused on young nearby stellar associations, the authors observed that the percentage of structured circumstellar disks (defined as featuring gaps, cavities, and rings, as opposed to compact disks that are largely unstructured) increases with stellar mass. Below  $M_{\star} = 1M_{\odot}$ , compact disks were found to represent 75%–90% of all observed disks, while for more massive stars, structured disks were observed in 50%–60% of the cases. Because structured disks tend to be more extended than compact disk and the dust radius is comparatively found at larger distances from the stars, these disks would move quickly past the detection threshold in the near- to mid-IR diagnostics that are used here to identify disk-bearing sources. This picture

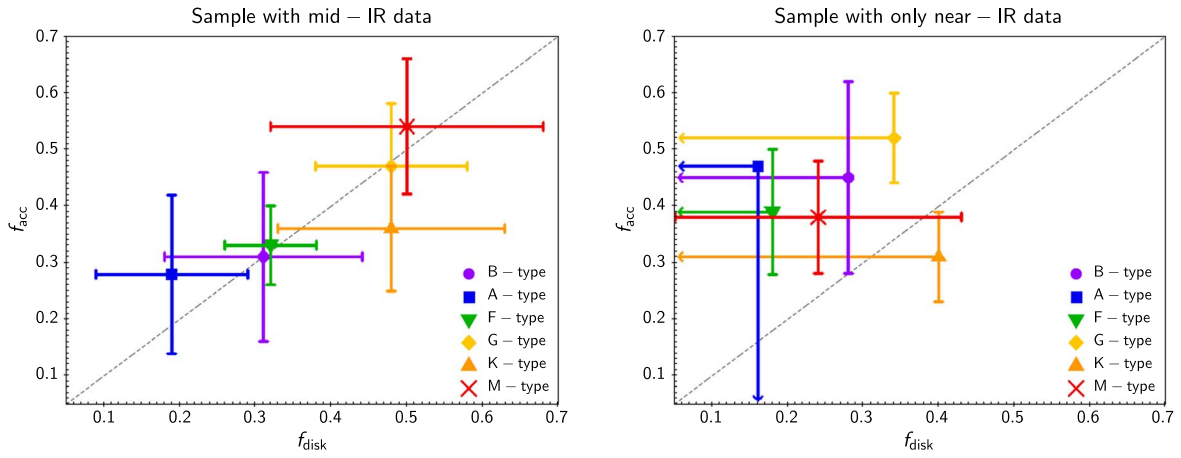


**Figure 10.** Comparison between the statistical SpT-dependent fractions of disk-bearing and accreting stars measured for the Lagoon Nebula population, as estimated from the subset of objects with disk classifications based on Spitzer/IRAC data (left) and on the subset for which only near-IR  $J$ ,  $H$ ,  $K$  data were available (right). O-type stars do not appear in the diagrams because no definite estimate of  $f_{\text{disk}}$  could be extracted for them. The arrows denote upper limits, and the equality line is dotted in gray.

is also qualitatively consistent with the statistically higher detection rate of disks around lower-mass stars than around high-mass stars that we derived for the Lagoon Nebula.

## 7.2. Environmental Feedback on Disk Evolution

To explore any local variations in the proportion of disk-bearing and accreting stars, we divided the field of view into  $0.05$  wide (R.A., decl.) bins on each side, and within each bin, we counted the fraction of objects classified as either disk-bearing or disk-free and either accreting or nonaccreting. To minimize any selection biases on disk-bearing sources, we limited this analysis to the sample of objects with mid-IR data available for the disk classification. We then retained all bins with three or more projected members to build a map of the frequency of disk activity across the Lagoon Nebula.

Our results are illustrated in Figure 11. In the top panel, a nonuniform spatial pattern appears in the local fraction of disk-bearing stars with respect to disk-free sources ( $f_{\text{disk}} - f_{\text{evolved}}$ ). At the heart of NGC 6530, within 1–2 parsec around the central coordinates of the O/B population at (R.A., decl.)  $\sim(271.01, -24.35)$ , disk-free or evolved disk sources appear to be statistically as numerous, if not more abundant, with respect to more primordial disks that can be detected at  $1\text{--}12\ \mu\text{m}$  wavelengths. The balance between disk-bearing and accreting stars instead appears to be more constant throughout the same region, with a measured  $f_{\text{acc}}$  similar to the local  $f_{\text{disk}}$  (middle panel of Figure 11). A potential overabundance of disk-bearing stars with respect to more evolved stars may emerge along the southwest edge of the cluster, between (R.A., decl.)  $\sim(271.0, -24.45)$  and (R.A., decl.)  $\sim(270.9, -24.35)$ , and around a more detached agglomeration of members at (R.A., decl.)  $\sim(270.7, -24.28)$ . The latter location appears to be characterized by a prevalence of disk-bearing stars over accreting stars, as suggested by the color scale in the middle panel of Figure 11.

These trends seem to correlate at least qualitatively with the distinctive spatial distributions of accreting/disk-bearing versus nonaccreting/disk-free Lagoon Nebula members mapped in Prisinzano et al. (2019). These authors noted two separate locations around which very young accreting/disk-bearing members are preferentially concentrated: the first around (R.A., decl.)  $\sim(271.1, -24.37)$ , close to the location with the

highest concentration of massive stars in Figure 11, and the second following an elongated rim between (R.A., decl.)  $\sim(271.1, -24.47)$  and (R.A., decl.)  $\sim(270.9, -24.35)$ , which overlaps with the southwest cluster edge described above. The approximate boundary of the first overdensity region from Prisinzano et al. (2019), as well as the lower envelope for the second elongated locus, is drawn in all panels of Figure 11. Prisinzano et al. noted that while nonaccreting/disk-free objects are found in a more widespread distribution around the center of the NGC 6530 cluster (and hence overlap with the first concentration of accreting/disk-bearing members), very few evolved members are found near the elongated rim. They suggested that these spatial properties are indicative of a sequential star formation history triggered by two distinct ionizing fronts, one at the center of the NGC 6530 cluster, and the other traced by the southwest rim.

A similar spatial analysis of the accretion intensity, illustrated in the bottom panel of Figure 11, also revealed some notable trends. Within a radius of  $\sim 1.2$  pc around (R.A., decl.)  $\sim(271.1, -24.38)$ , accreting cluster members typically display moderate  $\dot{M}_{\text{acc}}$  levels of  $\sim 5 \times 10^{-9} M_{\odot} \text{ yr}^{-1}$ . Higher typical  $\dot{M}_{\text{acc}}$  levels ( $\sim 1 \times 10^{-8} M_{\odot} \text{ yr}^{-1}$ ) are instead measured outside of this region and within a radius of  $\sim 3.5$  pc from the cluster center, with a peak  $\dot{M}_{\text{acc}} \sim 3 \times 10^{-8} M_{\odot} \text{ yr}^{-1}$  around the southwest location at (R.A., decl.)  $\sim(270.9, -24.4)$ . Comparable accretion rates  $\dot{M}_{\text{acc}} \sim 7\text{--}15 \times 10^{-9} M_{\odot} \text{ yr}^{-1}$  are also found around the western concentration of members at (R.A., decl.)  $\sim(270.7, -24.3)$ . Taken together, the lower disk fractions and accretion rates that are observed around the core of NGC 6530 with respect to its outer shell suggest that the intense radiation field produced by massive O/B stars at the heart of the region may impact the pattern and timescales of disk evolution. The combined effects of externally induced disk clearing and internal photoevaporation may lead to shortened disk lifetimes (e.g., Winter & Haworth 2022), as traced from dust emission diagnostics. Indeed, observational studies of other massive star-forming regions such as NGC 2244 (Balog et al. 2007), the Eagle Nebula (Guarcello et al. 2010), and Cygnus OB2 (Guarcello et al. 2023) have revealed a definite drop in the measured disk fractions within a radius  $\sim 0.5\text{--}1$  pc from the location of the highest-mass stars. At the same time, gas accretion can still continue at a detectable rate through the developing disk cavity (e.g., Gárate et al. 2021), possibly explaining the lack of a



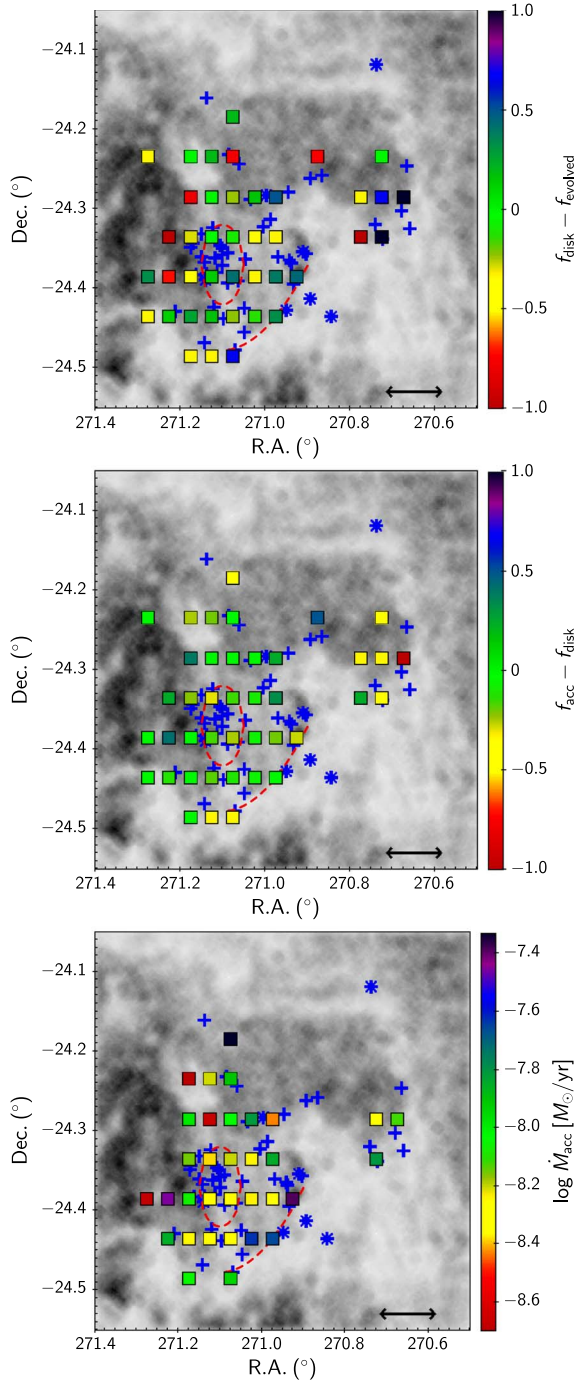


**Figure 11.** Spatial variations in the measured  $f_{\text{disk}}$ ,  $f_{\text{acc}}$ , and  $\dot{M}_{\text{acc}}$  in the Lagoon Nebula region (north is up, and east is to the left). In all panels, the background density map illustrates the distribution of point sources extracted from the VST/OmegaCAM images. The top panel shows local differences in proportion of disk-bearing ( $f_{\text{disk}}$ ) vs. disk-free ( $f_{\text{evolved}}$ ) sources when the field is divided into a grid of  $0^{\circ}05 \times 0^{\circ}05$  bins. Each bin is color-coded according to the measured  $f_{\text{disk}} - f_{\text{evolved}}$ , following the color scheme of the side axis. The middle panel shows the same field characterization where each bin is colored according to the local difference between  $f_{\text{acc}}$  and  $f_{\text{disk}}$ . The bottom panel illustrates local variations in the average measured  $\log \dot{M}_{\text{acc}}$ . In all diagrams, O- and B-type members are identified as blue asterisks and crosses, respectively. The double arrow in the bottom right corner marks a reference distance of 3 pc at the location of the Lagoon Nebula. The two dashed red contours indicate the spatial concentrations of the youngest Lagoon Nebula YSOs identified by Prisinzano et al. (2019).

drop of similar magnitude in  $f_{\text{acc}}$  in the middle panel of Figure 11 that would produce a color pattern matching the top diagram. An increased proportion of disk-bearing sources along the southwest

cluster boundary, in spite of it being similarly aged as the NGC 6530 core (Prisinzano et al. 2019), would then denote a reduced impact of external conditions on the local disk evolution pattern, with a potential restoration of the typical mutual ordering between accretion and disk dispersal timescales (with  $f_{\text{acc}}$  decreasing more quickly than  $f_{\text{disk}}$ ; e.g., Fedele et al. 2010; Venuti et al. 2018).

In order to test this scenario, we followed the prescriptions of Parravano et al. (2003) to derive a map of the local FUV flux induced by the distribution of O/B stars in Figure 11 and examined any potential correlations between the calculated flux levels and the observed variations in  $f_{\text{disk}}$  and  $f_{\text{acc}}$ . A direct comparison of these quantities is hampered by independent and competing factors such as age trends and age uncertainties in disk evolution or the mass dependence of the disk timescales, and no conclusive evidence could be extracted from our bidimensional analysis. However, when restricting this exploration to K-type stars (which constitute the only sufficiently numerous similar-mass subset in our sample to retain statistical representation after accounting for stellar age and spatial binning),  $f_{\text{disk}}$  values higher than 0.5 tend to be associated with local far-UV fluxes that are about 0.3 dex less intense than the typical estimate for spatial positions where the estimated  $f_{\text{disk}}$  is smaller than  $f_{\text{evolved}}$ . This tentative distinction emerges in particular at ages  $\gtrsim 1$  Myr, although the derived typical values for high- $f_{\text{disk}}$  and low- $f_{\text{disk}}$  locations would still be consistent within the associated scatter.

## 8. Summary and Conclusions

In this work, we have examined the properties and evolution of disk accretion in young stars in the Lagoon Nebula region. Our analysis was anchored on a sample of 1012 member YSOs, distributed in mass between  $\leq 0.2 M_{\odot}$  and  $\geq 5 M_{\odot}$ . We employed homogeneous simultaneous  $g$ ,  $r$ ,  $i$  photometry, obtained with VST/OmegaCAM, to determine the fundamental stellar properties for individual objects ( $A_V$ , SpT,  $M_{\star}$ ). We then combined the optical stellar colors with  $u$ -band and  $H\alpha$  flux measurements (also obtained at the same time with OmegaCAM) to detect and measure excess emission linked to mass accretion onto the star.

By using near- to mid-IR archival photometry, we estimated a statistical disk fraction  $f_{\text{disk}} \sim 0.34\text{--}0.37$  for our sample, which is consistent within the uncertainties with the derived fraction of YSOs with evidence of ongoing mass accretion,  $f_{\text{acc}} \sim 0.38\text{--}0.41$ . When broken down into spectral classes and disk diagnostics, statistically consistent values of  $f_{\text{disk}}$  and  $f_{\text{acc}}$  are measured for sources with a disk detection at mid-IR ( $3.6\text{--}8.0 \mu\text{m}$ ) wavelengths. On the other hand, the estimated fraction of accretors appears to be systematically larger than the fraction of disks detectable in the near-IR ( $1.2\text{--}2.2 \mu\text{m}$ ). This suggests ongoing inside-out disk clearing mechanisms that may be operating on quicker timescales around higher-mass (SpT < K) stars, although our surveyed population is estimated to be significantly incomplete at very low masses ( $M_{\star} \lesssim 0.5 M_{\odot}$ ). A close examination of spatial variations in the proportion of disk-bearing, disk-free, and accreting sources in the region suggests that dust depletion may occur more quickly for disks close to the core of NGC 6530, where the bulk of massive stars can be found. In the same area, the fraction of accreting stars appears to be similar to the fraction of disk-bearing stars, indicating that the quicker dust depletion does not immediately halt stellar gas accretion. Conversely, in

the outer areas of the region, particularly along the southwestern star formation front, the fraction of disk-bearing stars tends to exceed the fraction of accreting stars and that of disk-free stars, suggesting a more regular disk evolution timeline. This differential evolutionary pattern for disk-bearing YSOs in the core versus the outskirts of the region, in spite of their estimated similar ages, is also supported by the typical  $\dot{M}_{\text{acc}}$  values measured in the two areas, which are higher by a factor of two along the southwestern rim than in the cluster center.

The distribution of mass accretion rates as a function of stellar mass exhibits an overall correlation with at least one and potentially two break points in the relation: the first around  $M_{\star} \sim 1.02 M_{\odot}$ , and the second tentative one at  $M_{\star} \gtrsim 4.07 M_{\odot}$ . As reported in earlier studies of accretion variability in YSOs, the variability amplitudes on  $\dot{M}_{\text{acc}}$  detected here on timescales of a few weeks are statistically consistent with changes in the accretion rates measured over timescales of years for the same sources. This indicates that timescales of days to weeks typically dominate the dynamics of the targeted YSOs over baselines that are at least tens of times longer. The most erratic variables identified with K2 tend to exhibit higher  $\dot{M}_{\text{acc}}$  than the bulk of the population at a given mass; in addition, especially in the burster category, they tend to display a weaker  $\dot{M}_{\text{acc}}$  variability than the bulk of YSOs, which may indicate a more chaotic distribution of surface accretion shocks (leading to weaker modulation). The shocks themselves appear to be structured in density, leading to slightly asynchronous light curves in different filters and to potential differences in cycle duration as a function of wavelength. Indeed, a limited timing analysis of brightness phases from the  $u$  to the  $i$  band, compared to the simultaneous K2 light curves for accretion modulated stars, resulted in frequent lags being detected between the light curves in different filters. The measured delays are typically  $\sim 7\%$  of the optical light-curve period extracted from the K2 data, but can reach fractions as large as  $>30\%$ .

Additional factors such as stellar multiplicity can impact the evolutionary picture for the accretion disks examined here. Indeed, observational surveys conducted in other star formation environments have suggested that the presence of companions may lead to a rapid disk disappearance in the first few Myr of pre-main-sequence evolution (e.g., Harris et al. 2012), including dynamical disk disruptions that may trigger a quick depletion of the dust content in the inner disk (e.g., Francis & van der Marel 2020). To explore the connection between stellar multiplicity and inner disk dynamics, we have undertaken a survey of binary status for disk-bearing and disk-free young stars in the Lagoon Nebula that encompass a wide range of identified K2 variability behaviors. The results from that survey will be presented in a forthcoming paper (L. Venuti et al. 2024, in preparation).

### Acknowledgments










We thank the anonymous referee for their thorough review that helped us strengthen the presentation of our results. This work was supported by the National Aeronautics and Space Administration (NASA) under grant No. 80NSSC21K0633 issued through the NNH20ZDA001N Astrophysics Data Analysis Program (ADAP). L.V. warmly acknowledges the Centre for the Subatomic Structure of Matter for their hospitality during her stays at the University of Adelaide as a Visitor in 2022–2023. This research made use of Lightcurve,

Python package for Kepler and TESS data analysis (Lightcurve Collaboration et al. 2018), and Photutils, an Astropy package for detection and photometry of astronomical sources (Bradley et al. 2022). This publication makes use of data products from the Two Micron All Sky Survey, which is a joint project of the University of Massachusetts and the Infrared Processing and Analysis Center/California Institute of Technology, funded by NASA and the National Science Foundation. This publication also makes use of data products from the Wide-field Infrared Survey Explorer, which is a joint project of the University of California, Los Angeles, and the Jet Propulsion Laboratory/California Institute of Technology, funded by NASA. This work has also made use of data from the European Space Agency (ESA) mission Gaia (<https://www.cosmos.esa.int/gaia>), processed by the Gaia Data Processing and Analysis Consortium (DPAC, <https://www.cosmos.esa.int/web/gaia/dpac/consortium>). Funding for the DPAC has been provided by national institutions, in particular the institutions participating in the Gaia Multilateral Agreement.

*Facilities:* VST (OmegaCAM), Kepler/K2, Spitzer (IRAC).

*Software:* TOPCAT (Taylor 2005), SciPy (Virtanen et al. 2020), Photutils (Bradley et al. 2022).

### ORCID iDs

Laura Venuti  <https://orcid.org/0000-0002-4115-0318>  
 Ann Marie Cody  <https://orcid.org/0000-0002-3656-6706>  
 Giacomo Beccari  <https://orcid.org/0000-0002-3865-9906>  
 Luisa M. Rebull  <https://orcid.org/0000-0001-6381-515X>  
 Michael J. Irwin  <https://orcid.org/0000-0002-2191-9038>  
 Silvia H. P. Alencar  <https://orcid.org/0000-0002-5171-8376>  
 Geert Barentsen  <https://orcid.org/0000-0002-3306-3484>  
 Janet E. Drew  <https://orcid.org/0000-0003-1192-7082>  
 Steve B. Howell  <https://orcid.org/0000-0002-2532-2853>

### References

- Aigrain, S., Parviainen, H., & Pope, B. J. S. 2016, *MNRAS*, **459**, 2408
- Alcalá, J. M., Manara, C. F., Natta, A., et al. 2017, *A&A*, **600**, A20
- Alecian, E., Wade, G. A., Catala, C., et al. 2013, *MNRAS*, **429**, 1001
- Alexander, R. D., & Armitage, P. J. 2006, *ApJL*, **639**, L83
- Appelgren, J., Lambrechts, M., & Johansen, A. 2020, *A&A*, **638**, A156
- Arias, J. I., Barbá, R. H., & Morrell, N. I. 2007, *MNRAS*, **374**, 1253
- Arnaboldi, M., Capaccioli, M., Mancini, D., et al. 1998, *Msngr*, **93**, 30
- Balog, Z., Muzerolle, J., Rieke, G. H., et al. 2007, *ApJ*, **660**, 1532
- Barentsen, G., Vink, J. S., Drew, J. E., et al. 2011, *MNRAS*, **415**, 103
- Bastien, P. 2015, in *Polarimetry of Stars and Planetary Systems*, ed. L. Kolokolova, J. Hough, & A. Levasseur-Regourd (Cambridge: Cambridge Univ. Press), **176**
- Beccari, G., Spezzi, L., De Marchi, G., et al. 2010, *ApJ*, **720**, 1108
- Bell, C. P. M., Naylor, T., Mayne, N. J., Jeffries, R. D., & Littlefair, S. P. 2013, *MNRAS*, **434**, 806
- Bessell, M. S., Castelli, F., & Plez, B. 1998, *A&A*, **333**, 231
- Böhm-Vitense, E. 1981, *ARA&A*, **19**, 295
- Bonito, R., Prisinzano, L., Venuti, L., et al. 2020, *A&A*, **642**, A56
- Bouvier, J., Alencar, S. H. P., Harries, T. J., Johns-Krull, C. M., & Romanova, M. M. 2007, in *Protostars and Planets V*, ed. B. Reipurth, D. Jewitt, & K. Keil (Tucson, AZ: Univ. Arizona Press), **479**
- Ribas, Á., Bouy, H., & Merín, B. 2015, *A&A*, **576**, A52
- Bradley, L., Sipőcz, B., Robitaille, T., et al. 2022, *astropy/photutils*: v1.5.0, Zenodo, doi:10.5281/zenodo.6825092
- Briceño, C., Calvet, N., Hernández, J., et al. 2019, *AJ*, **157**, 85
- Brittain, S. D., Kamp, I., Meeus, G., Oudmaier, R. D., & Waters, L. B. F. M. 2023, *SSRv*, **219**, 7
- Broos, P. S., Getman, K. V., Povich, M. S., et al. 2013, *ApJS*, **209**, 32
- Calvet, N., & Gullbring, E. 1998, *ApJ*, **509**, 802
- Cardelli, J. A., Clayton, G. C., & Mathis, J. S. 1989, *ApJ*, **345**, 245
- Castro, P. J. 2013, PhD thesis, University of Delaware
- Chabrier, G. 2003, *PASP*, **115**, 763

- Chen, L., de Grijs, R., & Zhao, J. L. 2007, *AJ*, **134**, 1368
- Choi, J., Dotter, A., Conroy, C., et al. 2016, *ApJ*, **823**, 102
- Cody, A. M., & Hillenbrand, L. A. 2018, *AJ*, **156**, 71
- Cody, A. M., Hillenbrand, L. A., & Rebull, L. M. 2022, *AJ*, **163**, 212
- Cody, A. M., Stauffer, J., Baglin, A., et al. 2014, *AJ*, **147**, 82
- Coleman, G. A. L., & Haworth, T. J. 2022, *MNRAS*, **514**, 2315
- Costigan, G., Vink, J. S., Scholz, A., Ray, T., & Testi, L. 2014, *MNRAS*, **440**, 3444
- Damiani, F., Flaccomio, E., Micela, G., et al. 2004, *ApJ*, **608**, 781
- Damiani, F., Prisinzano, L., Micela, G., & Sciortino, S. 2006, *A&A*, **459**, 477
- Damiani, F., Prisinzano, L., Micela, G., & Sciortino, S. 2019, *A&A*, **623**, A25
- David, T. J., Hillenbrand, L. A., Gillen, E., et al. 2019, *ApJ*, **872**, 161
- De Marchi, G., Panagia, N., & Romaniello, M. 2010, *ApJ*, **715**, 1
- Dotter, A. 2016, *ApJS*, **222**, 8
- Drew, J. E., Gonzalez-Solares, E., Greimel, R., et al. 2014, *MNRAS*, **440**, 2036
- Eisner, J. A., Hillenbrand, L. A., & Stone, J. M. 2014, *MNRAS*, **443**, 1916
- Espaillet, C., Muzerolle, J., Najita, J., et al. 2014, in *Protostars and Planets VI*, ed. H. Beuther et al. (Tucson: University of Arizona Press), 497
- Espaillet, C. C., Robinson, C. E., Romanova, M. M., et al. 2021, *Natur*, **597**, 41
- Evans, N. J. I., Dunham, M. M., Jørgensen, J. K., et al. 2009, *ApJS*, **181**, 321
- Fairlamb, J. R., Oudmaijer, R. D., Mendigutia, I., Ilee, J. D., & van den Ancker, M. E. 2017, *MNRAS*, **464**, 4721
- Fazio, G. G., Hora, J. L., Allen, L. E., et al. 2004, *ApJS*, **154**, 10
- Fedele, D., van den Ancker, M. E., Henning, T., Jayawardhana, R., & Oliveira, J. M. 2010, *A&A*, **510**, A72
- Feigelson, E. D., Townsley, L. K., Broos, P. S., et al. 2013, *ApJS*, **209**, 26
- Fischer, W. J., Hillenbrand, L. A., Herczeg, G. J., et al. 2023, in *ASP Conf. Ser.* 534, *Protostars and Planets VII*, ed. Shu-ichiro Inutsuka et al. (San Francisco: CAASP)
- Flaccomio, E., Micela, G., Peres, G., et al. 2023, *A&A*, **670**, A37
- Francis, L., & van der Marel, N. 2020, *ApJ*, **892**, 111
- Fukugita, M., Ichikawa, T., Gunn, J. E., et al. 1996, *AJ*, **111**, 1748
- Gaia Collaboration, Prusti, T., de Bruijne, J. H. J., et al. 2016, *A&A*, **595**, A1
- Gaia Collaboration, Vallenari, A., Brown, A. G. A., et al. 2023, *A&A*, **674**, A1
- Gárate, M., Delage, T. N., Stadler, J., et al. 2021, *A&A*, **655**, A18
- Gilmore, G., Randich, S., Asplund, M., et al. 2012, *Msngr*, **147**, 25
- Gravity Collaboration, García López, R., Natta, A., et al. 2020, *Natur*, **584**, 547
- Gray, R. O., & Corbally, C. J. 2009, *Stellar Spectral Classification* (Princeton, NJ: Princeton Univ. Press)
- Guarcello, M. G., Drake, J. J., Wright, N. J., et al. 2023, *ApJS*, **269**, 13
- Guarcello, M. G., Micela, G., Peres, G., Prisinzano, L., & Sciortino, S. 2010, *A&A*, **521**, A61
- Gullbring, E., Hartmann, L., Briceño, C., & Calvet, N. 1998, *ApJ*, **492**, 323
- Harris, R. J., Andrews, S. M., Wilner, D. J., & Kraus, A. L. 2012, *ApJ*, **751**, 115
- Hartmann, L., Herczeg, G., & Calvet, N. 2016, *ARA&A*, **54**, 135
- Herczeg, G. J., & Hillenbrand, L. A. 2014, *ApJ*, **786**, 97
- Herczeg, G. J., & Hillenbrand, L. A. 2015, *ApJ*, **808**, 23
- Hernández, J., Hartmann, L., Megeath, T., et al. 2007, *ApJ*, **662**, 1067
- Hosokawa, T., Offner, S. S. R., & Krumholz, M. R. 2011, *ApJ*, **738**, 140
- Howell, S. B., Sobek, C., Haas, M., et al. 2014, *PASP*, **126**, 398
- Huber, D., Bryson, S. T., Haas, M. R., et al. 2016, *ApJS*, **224**, 2
- Jardine, M., Collier Cameron, A., Donati, J. F., Gregory, S. G., & Wood, K. 2006, *MNRAS*, **367**, 917
- Jester, S., Schneider, D. P., Richards, G. T., et al. 2005, *AJ*, **130**, 873
- Johnstone, C. P., Jardine, M., Gregory, S. G., Donati, J. F., & Hussain, G. 2014, *MNRAS*, **437**, 3202
- Jordi, K., Grebel, E. K., & Ammon, K. 2006, *A&A*, **460**, 339
- Kalari, V. M., Vink, J. S., Drew, J. E., et al. 2015, *MNRAS*, **453**, 1026
- Kenyon, S. J., & Hartmann, L. 1995, *ApJS*, **101**, 117
- Kimura, S. S., Kunitomo, M., & Takahashi, S. Z. 2016, *MNRAS*, **461**, 2257
- Koenig, X. P., & Leisawitz, D. T. 2014, *ApJ*, **791**, 131
- Kuijken, K. 2011, *Msngr*, **146**, 8
- Kuijken, K., Bender, R., Cappellaro, E., et al. 2002, *Msngr*, **110**, 15
- Kumar, D. L., & Anandarao, B. G. 2010, *MNRAS*, **407**, 1170
- Kurosawa, R., Harries, T. J., & Symington, N. H. 2006, *MNRAS*, **370**, 580
- Kurosawa, R., Romanova, M. M., & Harries, T. J. 2011, *MNRAS*, **416**, 2623
- Lada, C. J. 1987, in *IAU Symp.* 115, *Star Forming Regions*, ed. M. Peimbert & J. Jugaku (Berlin: Springer), 1
- Lavail, A., Kochukhov, O., Hussain, G. A. J., et al. 2017, *A&A*, **608**, A77
- Lightkurve Collaboration, Cardoso, J. V. d. M., Hedges, C., et al., 2018  
Lightkurve: Kepler and TESS time series analysis in Python, Astrophysics Source Code Library, ascl:1812.013
- Liu, B., Ormel, C. W., & Lin, D. N. C. 2017, *A&A*, **601**, A15
- Luhman, K. L., Stauffer, J. R., Muench, A. A., et al. 2003, *ApJ*, **593**, 1093
- Manara, C. F., Robberto, M., Da Rio, N., et al. 2012, *ApJ*, **755**, 154
- Manara, C. F., Testi, L., Rigliaco, E., et al. 2013, *A&A*, **551**, A107
- Matsakos, T., Chièze, J. P., Stehlé, C., et al. 2013, *A&A*, **557**, A69
- Mendigutia, I., Calvet, N., Montesinos, B., et al. 2011, *A&A*, **535**, A99
- Ribas, Á., Merín, B., Bouy, H., & Maud, L. T. 2014, *A&A*, **561**, A54
- Meyer, M. R., Calvet, N., & Hillenbrand, L. A. 1997, *AJ*, **114**, 288
- Morau, E., Bouvier, J., & Clarke, C. 2005, *AN*, **326**, 985
- Ordenes-Huanca, C., Zoccali, M., Bayo, A., et al. 2022, *MNRAS*, **517**, 6191
- Orlando, S., Sacco, G. G., Argiroffo, C., et al. 2010, *A&A*, **510**, A71
- Parravano, A., Hollenbach, D. J., & McKee, C. F. 2003, *ApJ*, **584**, 797
- Pecaut, M. J., & Mamajek, E. E. 2013, *ApJS*, **208**, 9
- Pogodin, M., Drake, N., Beskrovnyaya, N., et al. 2022, *Univ*, **7**, 489
- Povich, M. S., Busk, H. A., Feigelson, E. D., Townsley, L. K., & Kuhn, M. A. 2017, *ApJ*, **838**, 61
- Povich, M. S., Kuhn, M. A., Getman, K. V., et al. 2013, *ApJS*, **209**, 31
- Prisinzano, L., Damiani, F., Kalari, V., et al. 2019, *A&A*, **623**, A159
- Prisinzano, L., Damiani, F., Micela, G., & Sciortino, S. 2005, *A&A*, **430**, 941
- Prisinzano, L., Damiani, F., Micela, G., & Pillitteri, I. 2007, *A&A*, **462**, 123
- Randich, S., Gilmore, G., & Gaia-ESO Consortium 2013, *Msngr*, **154**, 47
- Rauw, G., Nazé, Y., Gosset, E., et al. 2002, *A&A*, **395**, 499
- Richert, A. J. W., Getman, K. V., Feigelson, E. D., et al. 2018, *MNRAS*, **477**, 5191
- Rigliaco, E., Natta, A., Randich, S., Testi, L., & Biazzo, K. 2011, *A&A*, **525**, A47
- Rilinger, A. M., Espaillet, C. C., Xin, Z., et al. 2023, *ApJ*, **944**, 66
- Robitaille, T. P., Whitney, B. A., Indebetouw, R., & Wood, K. 2007, *ApJS*, **169**, 328
- Romanova, M. M., Lii, P. S., Koldoba, A. V., et al. 2019, *MNRAS*, **485**, 2666
- Romanova, M. M., & Owocki, S. P. 2015, *SSRv*, **191**, 339
- Rosotti, G. P., Clarke, C. J., Manara, C. F., & Facchini, S. 2017, *MNRAS*, **468**, 1631
- Schmidt-Kaler, T. 1982, in *Stars and Star Clusters*, ed. K. Schaifers & H. H. Voigt (Berlin: Springer-Verlag)
- Skrutskie, M. F., Cutri, R. M., Stiening, R., et al. 2006, *AJ*, **131**, 1163
- Soderblom, D. R., Hillenbrand, L. A., Jeffries, R. D., Mamajek, E. E., & Naylor, T. 2014, in *Protostars and Planets VI*, ed. H. Beuther et al. (Tucson, AZ: Univ. Arizona Press), 219
- Sousa, A. P., Alencar, S. H. P., Rebull, L. M., et al. 2019, *A&A*, **629**, A67
- Sung, H., Chun, M.-Y., & Bessell, M. S. 2000, *AJ*, **120**, 333
- Taylor, M. B. 2005, in *ASP Conf. Ser.* 347, *Astronomical Data Analysis Software and Systems XIV*, ed. P. Shopbell, M. Britton, & R. Ebert (San Francisco, CA: ASP), 29
- Teixeira, P. S., Lada, C. J., Marengo, M., & Lada, E. A. 2012, *A&A*, **540**, A83
- Thanathibodee, T., Calvet, N., Hernández, J., Maucó, K., & Briceño, C. 2022, *AJ*, **163**, 74
- Tothill, N. F. H., Gagné, M., Stecklum, B., & Kenworthy, M. A. 2008, in *Handbook of Star Forming Regions, Volume II: The Southern Sky*, ASP Monograph Publications, Vol. 5 ed. B. Reipurth (San Francisco, CA: ASP), 533
- van den Ancker, M. E., The, P. S., Feinstein, A., et al. 1997, *A&AS*, **123**, 63
- van der Marel, N., & Mulders, G. D. 2021, *AJ*, **162**, 28
- Venuti, L., Bouvier, J., Flaccomio, E., et al. 2014, *A&A*, **570**, A82
- Venuti, L., Cody, A. M., Rebull, L. M., et al. 2021, *AJ*, **162**, 101
- Venuti, L., Prisinzano, L., Sacco, G. G., et al. 2018, *A&A*, **609**, A10
- Villebrun, F., Alecian, E., Hussain, G., et al. 2019, *A&A*, **622**, A72
- Vioque, M., Oudmaijer, R. D., Schreiner, M., et al. 2020, *A&A*, **638**, A21
- Vioque, M., Oudmaijer, R. D., Wichittanakom, C., et al. 2022, *ApJ*, **930**, 39
- Virtanen, P., Gommers, R., Oliphant, T. E., et al. 2020, *NatMe*, **17**, 261
- White, R. J., & Basri, G. 2003, *ApJ*, **582**, 1109
- Wichittanakom, C., Oudmaijer, R. D., Fairlamb, J. R., et al. 2020, *MNRAS*, **493**, 234
- Winter, A. J., & Haworth, T. J. 2022, *EPJP*, **137**, 1132
- Wright, E. L., Eisenhardt, P. R. M., Mainzer, A. K., et al. 2010, *AJ*, **140**, 1868
- Yang, H., & Johns-Krull, C. M. 2011, *ApJ*, **729**, 83